sustainability

MDPI

Article

Toward Sustainable E-Mobility: Optimizing the Design of Dynamic Wireless Charging Systems Through the DEXTER Experimental Platform

Giulia Di Capua [1,*], Nicola Femia [2], Antonio Maffucci [1], Sami Barmada [3] and Nunzia Fontana [3]

[1] Department of Electrical and Information Engineering, University of Cassino and Southern Lazio, 03043 Cassino, Italy; antonio.maffucci@unicas.it
[2] Department of Information and Electrical Engineering and Applied Mathematics, University of Salerno, 84084 Fisciano, Italy; femia@unisa.it
[3] Department of Energy, Systems, Territory, and Construction Engineering, University of Pisa, 56122 Pisa, Italy; sami.barmada@unipi.it (S.B.); nunzia.fontana@unipi.it (N.F.)
* Correspondence: giulia.dicapua@unicas.it

Abstract

Dynamic Wireless Power Transfer (DWPT) represents a promising solution to advance sustainable electric mobility by reducing vehicle downtime, extending driving range, and mitigating the need for battery oversizing. However, the lack of integrated and flexible experimental testbeds still limits the validation of emerging technologies. This paper presents DEXTER (Development of an Enhanced eXperimental proTotype of wirEless chargeR), a 1:2-scale open platform specifically designed for research on DWPT systems. The setup integrates a three-axis motion control for coil misalignments and trajectory emulation, digitally regulated TX/RX converters, a programmable battery emulator, and electromagnetic shielding coils equipped with field probes. A MATLAB-based interface enables automated testing and Hardware-in-the-Loop (HiL) integration. By combining modularity, scalability, and reproducibility, DEXTER provides a comprehensive framework for experimental optimization of power electronics and electromagnetic design while ensuring compliance with international safety standards. The case studies analyzed here demonstrate the capability of such a platform to validate and optimize the DWPT design choices, checking their impact on the overall performance of these systems. The platform constitutes a reference environment for both academia and industry, supporting the development of next-generation wireless charging systems and contributing to the sustainability and reliability of future electric mobility infrastructures.

Keywords: Wireless Power Transfer (WPT); dynamic wireless charging; Electric Vehicles (EVs); power electronics; electromagnetic shielding; mutual inductance modeling; Hardware-in-the-Loop (HiL); sustainable mobility

Academic Editors: Chao Gu, Chen-Chiung Hsieh and Pablo García Triviño

Received: 15 January 2026
Revised: 10 March 2026
Accepted: 19 March 2026
Published: 3 April 2026

1. Introduction

Wireless Power Transfer Systems (WPTSs) are increasingly recognized as key enablers of sustainable technologies, allowing contactless energy exchange in several domains, from biomedical implants and portable devices to large-scale transportation systems [1]. In the context of electric mobility, wireless charging eliminates the need for physical connectors and enables Dynamic Wireless Battery Charging (DWBC), where electric vehicles (EVs) can recharge while in motion. This paradigm can substantially reduce vehicle downtime,

extend driving range, and mitigate the environmental and economic costs associated with oversized battery packs [2]. In the broader context of sustainable mobility, Fuel Cell Vehicles (FCVs) also address range limitations and battery weight constraints through hydrogen-based energy storage and rapid refueling strategies, particularly in long-haul applications [3]. While FCVs rely on dedicated hydrogen infrastructure, DWBC offers an alternative electrification pathway that ensures energy in motion through grid-connected systems, potentially reducing battery oversizing without requiring on-board fuel storage.

Despite these advantages, achieving high system-level performance in terms of efficiency, compactness, and reliability remains challenging [4]. Dynamic charging infrastructure requires costly, complex installations, while the overall energy-efficiency-size-weight trade-off must be carefully optimized [5]. Advances in wide-bandgap (WBG) semiconductor devices, coil optimization, adaptive control, and electromagnetic shielding have significantly improved transfer efficiency, alignment tolerance, and electromagnetic compatibility. However, further progress requires a systemic approach that links device-level behavior with system-level design and control. In this regard, theoretical modeling must be complemented by experimental validation through hardware platforms that can reproduce realistic operating conditions. Such platforms should enable flexible test configuration, real-time parameter measurement, and integration of Hardware-in-the-Loop (HiL) logic to bridge the gap between modeling and experimentation. Most existing prototypes address only isolated subsystem issues, such as power electronics or coil design [6].

Most Wireless Power Transfer (WPT) prototypes reported in the literature focus on isolated subsystems rather than on end-to-end DWBC integration [7]. For instance, several prototypes are specifically designed for mutual-inductance optimization and coil design [8], receiver-side active power conditioning [9,10], or capacitive and hybrid compensation architectures, often validated only under simplified operating conditions [11]. Other platforms target individual functionalities, such as automated alignment [12], fault detection [13], thermal management [14], or electromagnetic compatibility (EMC) assessment [15,16], but still remain confined to subsystem-level evaluations. Consequently, the literature still lacks open, modular, and fully equipped testbeds that enable reproducible experiments on DWBC control strategies, behavioral models of magnetic components, and shielding solutions under realistic conditions.

This work presents the DEXTER platform (Development of an Enhanced eXperimental proTotype of wirEless chargeR), developed within the Italian PNRR Program MOST—Sustainable Mobility Center [17]. DEXTER provides a next-generation testbed for DWBC research, supporting comprehensive test scenarios such as resonance frequency detection, mapping of self- and mutual-inductance, and dynamic charging under controlled trajectory and speed profiles. The platform synthesizes and integrates the outcomes of several research activities developed over recent years on wireless power transfer systems, including:

- coil design and ferrite optimization, to improve coupling and reduce leakage flux [18–20];
- behavioral modeling of mutual and self-inductances, supporting data-driven parameter identification and model-based control [21–24];
- control-setting methodologies for system-level optimization and adaptive regulation under dynamic operating conditions [25–27];
- numerical shielding design, optimization, and prototyping [28,29].

DEXTER therefore establishes a unified experimental environment that supports the validation of analytical and numerical models, the development of advanced control strategies, the assessment of electromagnetic compliance and safety, and, more generally, the optimization of design choices with respect to targeted performance indicators.

Unlike commercially available wireless charging development kits, which are typically optimized for fixed coil geometries and predefined operating conditions, the DEXTER

platform has been conceived as a fully reconfigurable research-oriented testbed. Both the TX and RX control stages are digitally programmable and allow wide adjustment of switching frequency, RMS current reference, duty cycles, and equivalent load resistance, enabling systematic exploration of different performance targets. Furthermore, the platform supports automated 3D motion control for spatial mapping of resonance frequency and mutual inductance, integrated acquisition of electrical and magnetic-field quantities during dynamic operation, and Hardware-in-the-Loop (HiL) integration for behavioral model validation.

This high degree of configurability makes DEXTER suitable not only for functional validation but also for co-design studies involving electromagnetic modeling, control strategies, duty-cycle saturation analysis, and shielding optimization under realistic dynamic conditions.

Accordingly, the main contributions of this paper are: (*i*) to describe the architecture and functionalities of the DEXTER prototype; and (*ii*) to discuss experimental results validating both device-level and system-level models of DWBC systems. By providing an open, modular, and reproducible research framework, DEXTER supports both academia and industry in advancing the understanding and optimization of wireless charging technologies, thereby contributing to more efficient and sustainable electric mobility infrastructures.

The paper is organized as follows. Section 2 recalls the general aspects of DWBC systems, introducing a reference architecture and discussing the primary challenges associated with their design and analysis. Specific topics addressed include system-level modeling and performance-based design, electromagnetic behavioral modeling, and shielding design, as well as human exposure assessment. Section 3 presents the DEXTER prototype in detail, describing its architecture, experimental setup, and software–hardware integration. The subsequent sections illustrate selected experimental applications that demonstrate the capabilities of DEXTER. Section 4 focuses on validating the resonance frequency. Section 5 reports the validation of self- and mutual-inductance behavioral models. Section 6 presents the system performance validation results. Section 7 discusses the validation of the shielding coils. Finally, the concluding remarks summarize the main findings and outline future directions for extending the DEXTER platform to support advanced studies on electromagnetic exposure and sustainable e-mobility infrastructure.

2. Fundamentals of DWBC

To provide a reference framework for the design and analysis of DWBC systems, Figure 1 illustrates the schematic of a series–series compensated architecture, which has also been adopted in the development of the DEXTER prototype. This configuration, in fact, represents one of the most widely used topologies for both static and dynamic WPT applications.

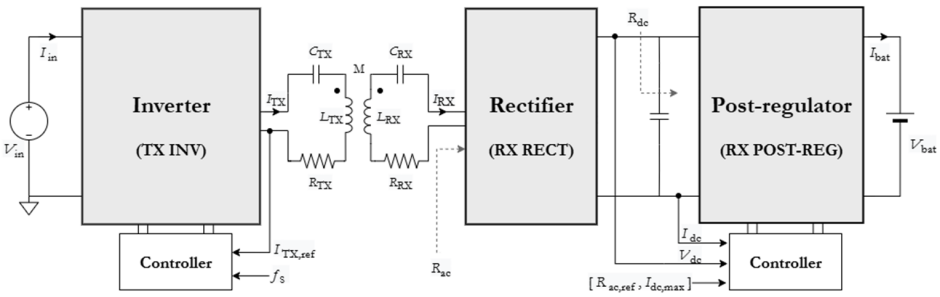

Figure 1. Reference DWBC architecture. The specific component values and electrical parameters adopted in the DEXTER experimental setup are detailed in Section 3.

In this reference system, the transmitter (TX) section includes a DC–AC inverter (TX INV) that regulates the root-mean-square (rms) current I_{TX} flowing through the TX coil, in order to achieve the desired reference value $I_{TX,ref}$. On the receiver (RX) side, a DC–DC post-regulation converter (RX POST-REG) controls the equivalent input resistance $R_{ac} = (8/\pi^2)R_{dc}$ seen by the rectifier (RX RECT), driving it toward a reference value $R_{ac,ref}$ corresponding to the selected load condition. The inductances of the TX and RX coils (L_{TX} and L_{RX}) are compensated by capacitors C_{TX} and C_{RX}, respectively, to ensure resonance at the operating frequency f_s set by the TX inverter. The total series resistances R_{TX} and R_{RX} include the coil ohmic losses and the equivalent series resistance of the compensation capacitors. This reference model provides the analytical basis for the performance evaluation and experimental validation discussed in the following sections.

2.1. System-Level Modeling

The key aspects concerning the performance analysis and design of a DWBC system based on the reference series-series compensated architecture, as shown in Figure 1, were thoroughly discussed in [27]. That study introduced the fundamental equations describing the constraints among the main reference parameters: the transmitter current setpoint $I_{TX,ref}$ controlled by the TX INV converter and the receiver equivalent load reference $R_{ac,ref}$ regulated by the RX POST-REG converter (see Figure 1), the spatial map of mutual inductance between TX and RX coils, the trajectory and speed of the moving RX coil, and the target performance indices in terms of transferred energy and overall charging efficiency.

The fundamental contribution of [27] was the formulation of performance-based design criteria derived from a behavioral mathematical model of the mutual inductance $M(x)$ between the TX and RX coils. These criteria enable the definition of design targets depending on specific goals, such as maximizing efficiency, energy throughput, or charging efficacy, while accounting for the geometric and electromagnetic characteristics of the coupling system.

Figure 2 schematically illustrates the relative motion of an RX coil (red rectangle) hosted by the vehicle with respect to a TX coil (blue rectangle), assuming the reference motion (nominal trajectory) for which the RX coil center moves along the longitudinal axis of the TX one (here denoted as the x-axis). Specifically, the figure shows three relative positions: in two, the RX coil is completely outside the TX coil, and in the third, the coils' centers are perfectly aligned. As the TX moves along this nominal trajectory, the mutual inductance $M(x)$ varies continuously, generating characteristic profiles whose shape depends on the coil geometry, number of turns, and the material and configuration of the other elements of the pads, such as magnetic ferrites and/or conducting shields [19,20].

In [27], the following dimensionless parameter was introduced to normalize the coupling behavior:

$$m(x) = \frac{[2\pi f_s M(x)]^2}{R_{TX} R_{RX}} \quad (1)$$

where $m(x)$ represents the normalized mutual inductance, defined as the ratio between the position-dependent mutual inductance $M(x)$ and the TX and RX series resistance R_{TX} and R_{RX} (including the ESR of coils and compensation capacitors). This parameter was used to establish the performance-based design equations of the DWBC system, showing that its peak and mean values, m_{pk} and m_{av}, along the RX trajectory must be properly correlated with the normalized load resistance $r_{ac,ref} = R_{ac,ref}/R_{RX}$, the transmitter current reference $I_{TX,ref}$, and the RX motion speed s_{RX}.

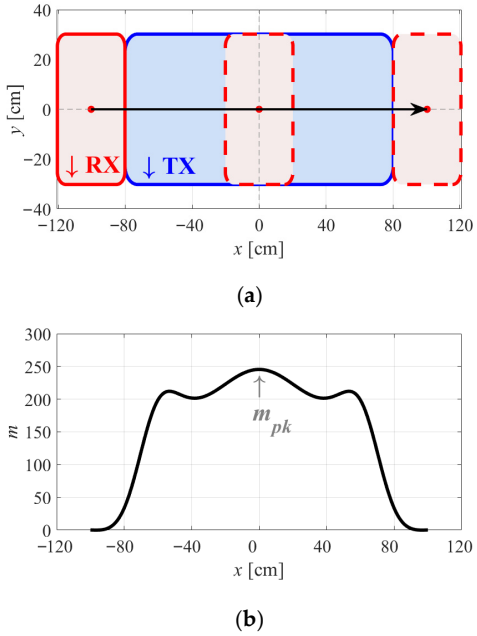

Figure 2. (**a**) TX and RX coils reciprocal position during RX coil motion over TX coil, assuming the nominal trajectory, and (**b**) typical resulting mutual inductance profile.

These correlations determine the attainable trade-off among efficiency, energy transfer, and charging performance. Furthermore, all the parameters influencing $m(x)$, namely the operating frequency f_s, the mutual inductance M, and the equivalent resistances R_{TX} and R_{RX}, are subject to inherent uncertainties arising from material properties, manufacturing tolerances, temperature variations, and the accuracy of the power converter regulators. These uncertainties directly affect predictions of resonance and efficiency, making experimental validation on controlled test platforms essential for verifying theoretical models and optimizing system-level design settings. In addition to these uncertainties, analytical modeling of WPT systems typically relies on simplifying assumptions that further affect the accuracy of performance predictions, namely, perfect resonance and unsaturated inverter operation.

A first common assumption in the modeling of WPT systems is, in fact, that the resonance condition is perfectly satisfied throughout operation. In practice, however, this assumption is only approximately valid. The self-inductances of the TX and RX coils, L_{TX} and L_{RX}, exhibit unavoidable variations caused by both their physical characteristics and the relative position of the RX coil with respect to the TX coil. Similarly, the compensation capacitors, C_{TX} and C_{RX}, show parameter drift due to temperature, frequency, and voltage-dependent behavior. As a result, the actual resonance frequency f_r of a WPT system is affected by a non-negligible degree of uncertainty influenced by these factors. Ensuring that a DWBC system truly achieves the intended performance targets, therefore, requires experimental validation of the models for $M(x)$, $L_{TX}(x)$, and $L_{RX}(x)$, as well as verification of the corresponding compensation capacitances C_{TX} and C_{RX}. These validations can be carried out through precise experimental measurements of the spatial profiles of the resonance frequency $f_r(x)$ and mutual inductance $M(x)$, as enabled by the DEXTER prototype described in Section 3.

A second fundamental assumption affecting the system-level performance of a DWBC system concerns the operation of the TX INV converter, specifically the possibility of duty-cycle saturation. Figure 3 shows the representative waveforms of the inverter output voltage and current.

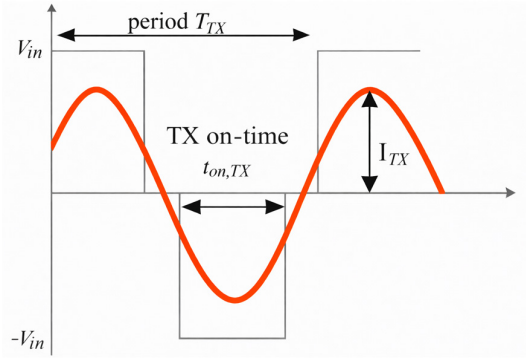

Figure 3. Waveforms of the inverter output voltage and current.

The TX INV converter sets the switching period $T_{TX} = 1/f_r$, where f_r denotes the common resonance frequency of the TX and RX circuits, and regulates the amplitude of the sinusoidal current I_{TX} to achieve the reference value $I_{TX,ref}$ corresponding to the desired DWBC performance target. The condition $I_{TX} = I_{TX,ref}$ can only be achieved if the inverter duty-cycle satisfies $0 \leq D_{TX} \leq 1$. According to [27], the duty-cycle D_{TX} varies along the RX trajectory as given in (2):

$$D_{TX}(x) = \frac{2}{\pi} arcsin\left[\frac{\pi R_{TX} I_{TX,ref}}{4V_{in}}\left(1 + \frac{m(x)}{1 + r_{ac,ref}}\right)\right] \tag{2}$$

This expression highlights that, for given system parameters and converter ratings, D_{TX} may reach its upper limit ($D_{TX} = 1$) during certain intervals of the RX motion, leading to inverter control saturation. Therefore, in real DWBC systems, the condition $D_{TX} < 1$ may be violated: local peaks of $m(x)$ or high current settings can push D_{TX} to reach its upper limit ($D_{TX} = 1$), resulting in saturation and loss of current regulation. This phenomenon directly affects power transfer and efficiency and can therefore be experimentally characterized.

The RX load regulation is achieved through the RX POST-REG converter, which sets the duty-cycle D_{RX} according to the desired normalized load reference $r_{ac,ref}$. Regulation is maintained if $0 \leq D_{RX} \leq 1$.

According to [27], for the RX POST-REG buck converter, we have:

$$D_{RX} = \frac{4}{\pi}\frac{V_{bat}}{I_{TX,ref}}\frac{1}{\sqrt{R_{TX}R_{RX}}}\frac{1}{\sqrt{m(x)}}\left(1 + \frac{m(x)}{r_{ac,ref}}\right) \qquad if\ D_{TX} < 1 \tag{3a}$$

$$D_{RX} = \frac{V_{bat}}{V_{in}}\sqrt{\frac{R_{TX}}{R_{RX}}}\frac{1}{\sqrt{m(x)}}\left(1 + \frac{1 + m(x)}{r_{ac,ref}}\right) \qquad if\ D_{TX} = 1 \tag{3b}$$

where V_{bat} is the battery voltage. Finally, the power delivered to the battery and the DWBC efficiency are given by [27]:

$$P_{bat} = \frac{8\ V_{bat}V_{in}}{\pi^2}\sqrt{\frac{R_{TX}}{R_{RX}}}\frac{sin\left(\frac{\pi}{2}D_{TX}\right)}{D_{RX}}\frac{\sqrt{m(x)}}{1 + m(x) + r_{ac,ref}} \tag{4}$$

$$\eta = \frac{m_{av}\ r_{ac,ref}}{\left(1 + m_{av} + r_{ac,ref}\right)\left(1 + r_{ac,ref}\right)} \tag{5}$$

where m_{av} is the average value of m over the vehicle trajectory. In fact, during the vehicle transit over the TX coil, the value of $m(x)$ varies from a minimum value (when the RX coil starts overlapping the TX coil) to a maximum value (named as peak value, m_{pk}), and returns to a minimum value again (when the RX coil ends overlapping the TX coil).

Equations (2)–(5) show that the saturation of D_{TX} directly influences D_{RX} and the battery power rate. Figure 4 compares the variations of D_{TX} (blue) and D_{RX} (red), as given by (1) and (7), along the RX trajectory for two different combinations of $I_{TX,ref}$ and $r_{ac,ref}$: one preventing and one inducing duty-cycle saturation. When D_{TX} remains below saturation (see Figure 4a), both converters exhibit smooth control behavior, simplifying system regulation. Conversely, when D_{TX} reaches its limit (see Figure 4b), steeper transients occur in both duty cycles, leading to reduced controllability and reduced efficiency.

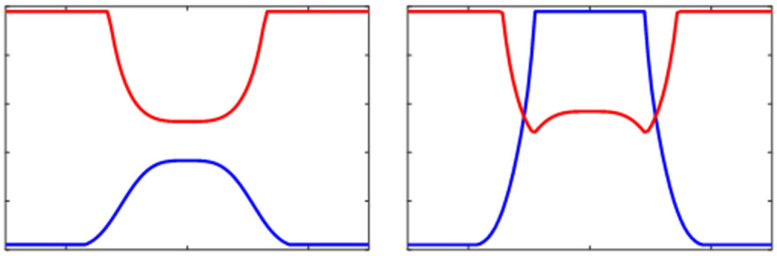

(**a**) (**b**)

Figure 4. D_{TX} (blue line) and D_{RX} (red line) while the RX coil moves over the TX coil, in the case of (**a**) non-saturated D_{TX} and (**b**) saturated D_{TX}.

Based on the analytical relationships above, the following observations can be made.

- D_{TX} increases with $I_{TX,ref}$ (see Equation (2)): hence, for higher m_{pk}, a lower $I_{TX,ref}$ must be selected to avoid saturation.
- Higher D_{TX} increases P_{bat} (see Equation (4)); thus, slight saturation can be beneficial for maximizing instantaneous power transfer. Accordingly, it might be advantageous to set $I_{TX,ref}$ higher, so that D_{TX} saturates for values of $m(x)$ lower than m_{pk}.
- Lowering $r_{ac,ref}$ appears to increase the battery power rate (see Equation (4)), but may raise D_{RX} (see Equation (3)), which in turn reduces the battery power rate.
- Increasing $I_{TX,ref}$ reduces D_{RX} (see Equation (3a)) and consequently enhances power transfer (see Equation (4)), provided D_{TX} does not saturate.
- Maximum efficiency is achieved when $r_{ac,ref} = \sqrt{1 + m_{av}}$ (see Equation (5)).

The management of TX inverter duty-cycle saturation definitely represents a key design aspect for system-level optimization. If the design priority is to maximize the charging power rate, it is advantageous to select $I_{TX,ref}$ and $r_{ac,ref}$ so that D_{TX} remains saturated for as long as possible during the RX coil transit, while keeping D_{RX} unsaturated and as low as feasible. By taking the optimal settings identified in [27] as a reference solution for the performance trade-off, the DEXTER platform enables experimental verification of this operating condition and supports fine-tuning of the reference pair $\{I_{TX,ref}, r_{ac,ref}\}$ required for real DWPT implementations to achieve the desired system-level objective. Indeed, given uncertainties in system parameters (such as variations in resonance frequency along the trajectory, parameter tolerances, and practical limits on D_{TX} imposed by MOSFET drivers), the actual performance may deviate from model predictions. Therefore, the optimal settings of switching frequency and reference control pair $\{I_{TX,ref}, r_{ac,ref}\}$ can only be determined and validated through experimental testing.

The DEXTER prototype enables automated execution of such tests, as illustrated in Section 3.

2.2. Electromagnetic Behavioral Modeling

The mutual inductance M plays a crucial role in determining both the energy transfer and efficiency of a DWBC system [27]. Its spatial profile $M(x)$ along the RX nominal

trajectory over the TX coil also affects the bandwidth requirements of the control systems that drive the duty cycles of the TX INV and RX POST-REG converters [22].

The most relevant features of the $M(x)$ curve are the rising and falling slopes when the RX coil approaches and leaves the TX coil and its flatness while the RX coil transits over the TX region. These characteristics depend on the geometry of the two windings (width, length, number of turns) and on the presence, shape and distribution of the other components of the magnetic pads, such as ferrite beds or conducting shields. TX and RX coils in air (without ferrites and shields) typically exhibit a wavy shape of $M(x)$, as shown in Figure 5a, whereas the adoption of magnetic pads yields a smoother mutual inductance profile, as shown in Figure 5b and discussed in [18]. Furthermore, segmented ferrite pads can be arranged to reduce the slope of the rising and falling edges of $M(x)$, improving coupling uniformity and reducing dynamic variations [20].

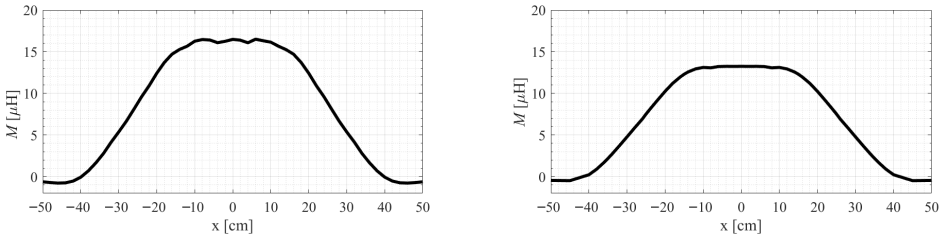

(**a**) (**b**)

Figure 5. Plot of $m(x)$ coil during the RX coil motion over TX coil: (**a**) coils without ferrites, (**b**) coils with ferrites.

Sharper variations and oscillatory profiles of $M(x)$ increase the dynamic range of the coupling coefficient, complicating the regulation of I_{TX} and R_{ac}, especially at high RX coil speeds s_{RX}. Consequently, a wider control bandwidth is required for both converters (TX INV and RX POST-REG) to maintain regulation during motion. To support control design, a behavioral mathematical representation of $M(x)$ is required, enabling the fine-tuning of control laws based on realistic magnetic coupling profiles.

Recent works have proposed detailed analytical formulations for computing the self- and mutual inductances of rectangular coils across a wide range of configurations, including misalignment scenarios [30,31]. Their main drawback, however, is that these approaches rely on highly complex multidimensional integrals, which make their practical adoption challenging and limit their use in WPT design and optimization workflows.

In contrast, the approach presented in [21,22] proposes a behavioral analytical model that preserves accuracy while drastically simplifying the mathematical structure. Instead of complex integral formulations, the mutual inductance is expressed through compact and easily evaluable closed-form expressions, capturing the dependence of M on the real TX–RX displacement. This yields a model that is straightforward to implement in standard circuit simulators (e.g., PSIM, Simulink), computationally lightweight, suitable for iterative design loops, and directly employable in EMC and human-exposure analyses for dynamic WPT systems. The key advantage, therefore, is the ability to retain the physical behavior of the magnetic link while avoiding the computational burdens associated with full analytical or FEM-based formulations.

As a representative case study, the coil pair shown in Figure 6 was analyzed to characterize the mutual inductance as a function of RX coil displacement. Both TX and RX coils include ferrite pads placed above the windings, facing each other with the ferrite layers located on the outer sides of the WPT structure. These coils were designed through a multi-objective optimization process [20], aimed at achieving a trade-off among minimizing ferrite volume, obtaining a flat M(x) profile along the RX trajectory, maximizing mutual

inductance, and minimizing magnetic flux leakage. This optimization was achieved by segmenting the ferrite pads into small plates, arranged as shown in Figure 6, which, overall, illustrates the reference geometry of the coil pair in three-dimensional space in an isometric view. Each RX position can be described by the coordinates (x,y,z) of its center relative to the TX coil center at (0,0,0). Accordingly, the mutual inductance can be expressed as a function $M(x,y,z)$ of the three-dimensional relative displacement between the coils.

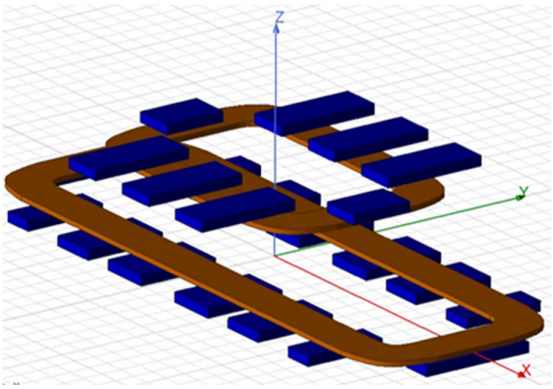

Figure 6. Coil pair reference geometry, isometric view.

Different case studies were analyzed, including: (a) nominal trajectory, when the RX coil moves along the TX longitudinal axis x; (b) parallel trajectories, when the RX coil laterally shifted along the y-axis with respect to the nominal path; and (c) elevated trajectories, corresponding to (a) and (b) at different vertical separations z between coil centers [24]. For each configuration, a discrete set of displacements (x,y,z) was used to compute the reference values of $M(x,y,z)$ for behavioral model identification. The coil pair was analyzed under Magneto-Quasi-Static (MQS) conditions using Ansys Maxwell 2024 R2. The FEM simulations were performed accounting for the B-H characteristics of the adopted ferrite material. However, under the excitation levels considered for the DEXTER prototype, the selected N27 ferrite (relative permeability $\mu_r \approx 2000$, saturation flux density $B_S \approx 500$ mT at 25 °C [24]) operates well below its saturation region. The resulting flux densities remain far from the magnetization curve's nonlinear knee, so the material behaves quasi-linearly over the investigated range. Consequently, no additional nonlinear correction terms are required in the behavioral inductance models.

The finite-element mesh was refined to ensure a maximum error of less than 3% in the evaluation of mutual inductance. The simulated data $M_{sim}(x,y,z)$ were then used as input for deriving a behavioral model M_{bhv}, according to the methodology described in [24]. The behavioral model was identified using MATLAB R2024b's Curve Fitting Toolbox (CFTool). Figure 7 presents a representative screenshot of the fitting workflow used to derive the model from the simulated mutual inductance data $M_{sim}(x,y,z)$. In fact, Figure 7 is intended as an overview of the tool interface rather than a detailed view of the results.

The adopted model structure is expressed as:

$$M_{bhv(x,y,z)} = a_0 \, exp\left(a_1|x|^{a_2} + a_3|y|^{a_4}\right) \quad (6)$$

where x and y are expressed in meters, and the M_{bhv} value is expressed in μ-Henries. The numerical coefficients a_i (i = 0,. . .,4), estimated using nonlinear least-squares optimization over the training dataset [24], were then expressed as a function of the vertical displacement Δz according to (7):

$$a_i = p_{i0} + p_{i1}\, z + p_{i2}\, z^2 \quad (7)$$

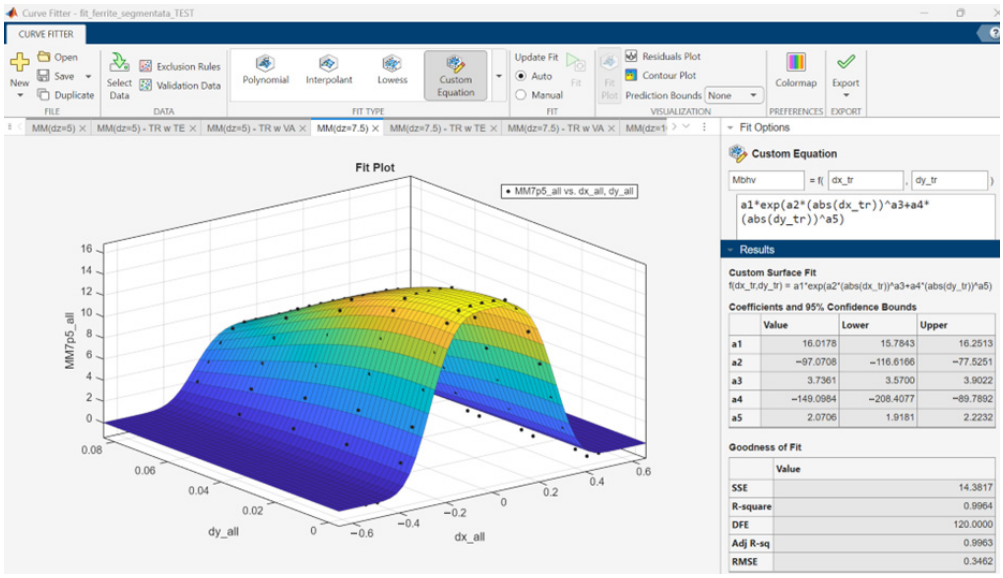

Figure 7. Overview screenshot of MATLAB CFTool used to perform the behavioral model fitting based on simulated mutual inductance data $M_{sim}(x,y,z)$.

A comprehensive description of the dataset generation procedure, the sampling density over the displacement space, the nonlinear least-squares fitting methodology, the validation strategy, and the convergence assessment is provided in [24], where the detailed regression and robustness analyses are extensively discussed. The accuracy of the proposed behavioral model has been previously assessed through a combined numerical and experimental validation campaign [24]. In particular, coefficient identification based on FEM-generated datasets yielded R^2 values close to 0.99 and RMSE values below 1 µH across the investigated displacement range. In the operating region corresponding to effective power transfer (i.e., moderate longitudinal and lateral misalignments), the relative errors remain typically within 5–10%. From a control perspective, this level of accuracy is compatible with real-time current-regulated control strategies in dynamic DWPT systems, where regulation loops are activated only above a minimum coupling threshold. The adopted closed-form model, therefore, represents a suitable trade-off between computational simplicity and predictive reliability for control-oriented applications.

A similar behavioral modeling methodology was applied to the self-inductances of the TX and RX coils, denoted as $L_{TX,bhv}$ and $L_{RX,bhv}$, respectively. These models were derived using the data-driven nonlinear fitting approach described in [32], which aims to capture the relationship between self-inductance and the relative coil displacements (x, y, z). The adopted model structures are expressed as:

$$L_{TX,bhv(x,y,z)} = b_0\, exp\left(b_1|x|^{b_2} + b_3|y|^{b_4}\right) + b_5 \tag{8a}$$

$$L_{RX,bhv(x,y,z)} = c_0\, exp\left(c_1|x|^{c_2} + c_3|y|^{c_4}\right) + c_5 \tag{8b}$$

where x and y are expressed in meters, and $L_{TX,bhv}$ and $L_{RX,bhv}$ values are expressed in µ-Henries. The coefficients b_i and c_i ($i = 0, \ldots, 5$) were estimated using nonlinear least-squares optimization over the training dataset [32], and again were expressed as a function of the vertical displacement Δz according to (9):

$$b_i = s_{i0} + s_{i1}\, z + s_{i2}\, z^2 \tag{9a}$$

$$c_i = t_{i0} + t_{i1}\, z + t_{i2}\, z^2 \tag{9b}$$

The results presented in [32] demonstrate that the proposed behavioral modeling framework for inductance identification and validation represents an effective and generalizable tool for supporting the reliable design of WPT systems. Several noteworthy aspects emerge from the analysis of the models identified for both mutual and self-inductances. First of all, the mathematical expressions for the mutual and the self-inductances share the same functional form, differing only in the constant coefficients b_5 and c_5, which represent the stand-alone self-inductance values of the TX and RX coils, respectively. This structural similarity confirms the robustness and generality of the proposed modeling approach, which can be readily extended to multiple TX–RX coil pairs by simply re-tuning the model coefficients through nonlinear least-squares optimization using simulation or experimental datasets. Moreover, the identified models indicate that the self-inductance values increase when the RX coil is positioned directly above the TX coil, compared to their stand-alone conditions. Consequently, tuning the compensation capacitors C_{TX} and C_{RX} solely based on stand-alone inductance values, as is commonly done in conventional WPT designs, may result in partial loss of resonance at positions where magnetic coupling is strongest and accurate tuning is most critical. Considering the nearly standardized spacing between RX and TX coils in most WPT configurations, the model coefficients of Equations (7) and (9) can be determined at a fixed vertical displacement z for different winding geometries and ferrite arrangements. This feature facilitates the identification and optimization of coil configurations tailored to the performance targets of specific WPT applications.

Overall, extending the behavioral modeling framework to self-inductances significantly enhances the predictive capability of the DWBC electromagnetic model. It enables the accurate estimation of the resonance frequency fr, dynamic coupling coefficients, and overall energy transfer characteristics, serving as the reference for both control strategy design and experimental validation using the DEXTER platform.

2.3. Shielding Design

A key challenge in the design of shielding systems for wireless power transfer applications is reducing magnetic fields in specific regions without compromising power transfer performance. With specific attention to vehicular systems, the high-power levels (in the order of kW) and large air gaps (in the order of centimeters) result in significant Magnetic Flux Leakage (MFL) that extends beyond the power transfer zone. This stray field, where human operators could be located, poses potential health risks and requires compliance with safety standards set by organizations such as IEEE and ICNIRP [33,34]. Additionally, the MFL can cause electromagnetic interference (EMI), affecting sensitive vehicle electronics, external devices, and medical implants, thereby raising significant EMC concerns [35].

WPT system's shielding techniques can be grouped into three main categories: passive methods based on conductive and/or magnetic materials [36], active approaches [37] and other solutions relying on reactive resonant concepts or hybrid configurations [38]. In the literature, the use of metamaterials for shielding purposes is also investigated [39]. Ferrites, commonly used to enhance coupling between the transmitter and receiver, also attenuate the MFL but come with limitations in terms of weight, cost, and mechanical fragility. In addition, while both ferrite and aluminum provide broadband attenuation, they introduce Joule losses, which reduce the overall efficiency of the WPT system.

The shielding-coil design adopted in this work builds upon the methodologies proposed in [28,29] and in [40–42]. In line with these contributions, the focus is on passive shielding solutions that do not require an external power supply, thereby enabling a simpler, more practical implementation for DWBC systems. The shielding concept leverages metamaterial principles, where an array of resonant elements is engineered to operate as a single shielding

component and to be integrated into the existing DWPC architecture. The resulting structure is modular and scalable; moreover, by relying on a resonant array rather than bulky conductive plates, it may reduce the amount of metallic material required, with potential benefits for material use and overall shield mass. Such features are particularly attractive for industrial applications, especially in the automotive sector, where packaging constraints and component weight are key design drivers. In all the above-mentioned studies, prototyping and experimental validation are consistently carried out, given the critical role of shielding solutions in ensuring safety and electromagnetic compatibility. A meaningful assessment requires the co-presence of both the realistic system to be shielded and the shielding structure under representative operating conditions. In this respect, the DEXTER platform enables the replication and systematic investigation of this coupled scenario.

It is worth emphasizing that implementing shielding solutions involves several trade-offs. A primary limitation of this type of structure is its narrow-band behavior. Therefore, particular attention should be paid to the self-resonance frequency of each element in the array and its relationship with the WPT system's operating frequency. Another key design parameter is the quality factor of each resonator, which should be as high as possible to minimize ohmic losses and preserve overall system efficiency. Since the resonator-coil array operates in the very near-field region, the relative position with respect to the TX and RX coils, as well as the inter-element spacing, becomes critical. In addition, practical implementations typically impose compactness constraints, i.e., the shielding-coil array is arranged to be coplanar with the transmitting coil and to cover its full longitudinal extent. Finally, in practical vehicular implementations, the presence of the vehicle chassis (typically made of conductive lightweight materials such as aluminum alloys) may introduce additional eddy-current effects and slightly modify the local magnetic field distribution. However, because the ferrite-tile arrangement already mitigates the field above the WPT assembly, the qualitative shielding behavior and relative attenuation trends are not expected to be significantly altered. A detailed quantitative assessment would require a full-vehicle electromagnetic model, which is beyond the scope of the present work.

In the configuration considered in Figure 8, the shielding structure consists of an array of n resonant coils, each tuned by a series-connected capacitor. The array is placed on both sides of the system, parallel to the direction of motion of the RX coil with respect to the TX coil. The induced currents in the shield elements can be computed by applying Kirchhoff's Voltage Law (KVL), as described in [28], to the equivalent circuit model and its schematic representation shown in Figure 8a,b. To simplify the analysis, the mutual coupling among resonator coils and the coupling between each resonator and the receiver coil ($M_{r,k}$) are assumed to be negligible compared with the mutual coupling between the transmitter and the shield elements ($M_{t,k}$).

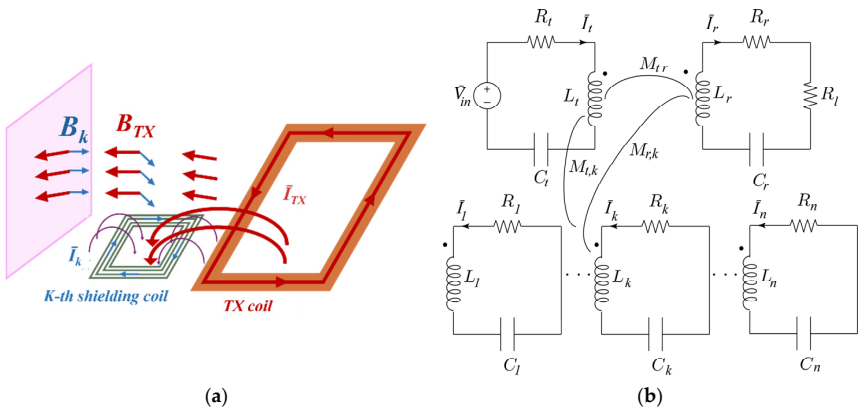

Figure 8. (**a**) Equivalent circuit of the WPT system with planar coil array shielding; (**b**) schematic representation of the magnetic field leakage suppression.

Consequently, M_{tr} and $M_{t,k}$ with $k = 1, \ldots, n$ are the most relevant quantities for the shield design, and the system reported in [28] is consequently simplified as in (10):

$$\begin{bmatrix} \dot{Z}_t & -j\omega M_{tr} & -j\omega M_{t,1} & \ldots & -j\omega M_{t,n} \\ -j\omega M_{tr} & \dot{Z}_r & -j\omega M_{r,1} & \ldots & -j\omega M_{r,n} \\ -j\omega M_{t,1} & -j\omega M_{r,1} & \dot{Z}_1 & & -j\omega M_{1,n} \\ \vdots & \vdots & \vdots & \ddots & \vdots \\ -j\omega M_{t,n} & -j\omega M_{r,n} & -j\omega M_{1,n} & \ldots & \dot{Z}_n \end{bmatrix} \begin{bmatrix} \bar{I}_t \\ \bar{I}_r \\ \bar{I}_1 \\ \vdots \\ \bar{I}_n \end{bmatrix} = \begin{bmatrix} \overline{V}_{in} \\ 0 \\ 0 \\ 0 \\ 0 \end{bmatrix} \tag{10}$$

where $_t$, $_r$, $_1$ and $_n$ are the impedance of the TX coil, the RX coil and the shielding coils, respectively. Equation (11) provides an analytical expression for the current $\bar{I}_k$ flowing in the kth shielding coil:

$$\bar{I}_k = \frac{j\omega M_{t,k}}{R_k + j\omega L_k \left(1 - \frac{\omega_k^2}{\omega^2}\right)} \bar{I}_t \tag{11}$$

where R_k and L_k denote the resistance and self-inductance of the k-th shielding coil, respectively; ω is the operating angular frequency of the WPT system and $\omega_k = 1/\sqrt{L_k C_k}$ is the self-resonant angular frequency of the k-th shielding coil. Introducing the quality factor of the k-th resonator $Q_k = (\omega_k L_k)/R_k$ and the coefficients $\alpha_k = M_{t,k}/L_k$ and $P_k = \omega_k/\omega$, Equation (11) can be rewritten in the compact form reported in (12):

$$\bar{I}_k = \frac{\alpha_k}{1 - P_k^2 - j\frac{P_k}{Q_k}} \bar{I}_t \tag{12}$$

Let us consider the simplified arrangement of the transmitting coil and the k-th coplanar shielding coil as shown in Figure 8. In the ideal case where the resonator resistance can be neglected ($R_k \approx 0$), Equation (11) reduces to:

$$\bar{I}_k = \frac{j\omega M_{t,k}}{j\omega L_k \left(1 - \frac{\omega_k^2}{\omega^2}\right)} \bar{I}_t \tag{13}$$

A normalized form of (13) can be easily represented by varying the normalized angular frequency factor, as reported in Figure 9. Considering the current directions shown in Figure 8a, the mutual inductance is positive ($M_{t,k} > 0$). Under this condition, a more effective shielding is obtained when the induced current in the shielding coil flows as indicated in the figure. In this case, the magnetic flux density vectors produced by the transmitting and shielding coils on the observation plane form an angle larger than 90°, leading to partial field cancellation and, consequently, to a reduced magnitude of the resulting flux density.

Therefore, the shielding performance of the resonant elements is mainly determined by the phase shift of the induced currents relative to the transmitting-coil current. To achieve the desired phase relationship, the shielding coils should be tuned to resonate at a frequency slightly higher than the WPT system's operating frequency.

In a realistic scenario, ohmic losses cannot be neglected. Accordingly, the main design parameters of the shielding array can be summarized as α_k, P_k and Q_k. The shielding array, modeled as a set of resonant coils, can be optimized by maximizing the magnitude of the induced current $\bar{I}_k$ in each element, as indicated by (12), and by adopting the following design criteria:

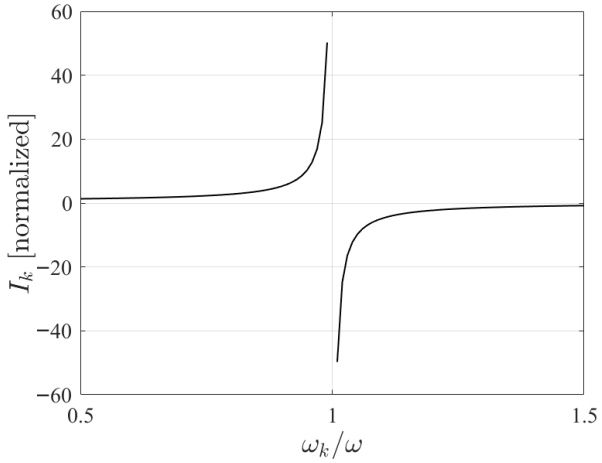

Figure 9. Induced current on the *k*-th shielding resonator according to the normalized angular frequency.

- α_k should be as large as possible, as it directly scales the induced current strength in the *k*-th shielding coil;
- P_k, the angular frequency ratio, should be close to unity and slightly greater than 1. This ensures that the induced current $\bar{I}_k$ lags the source current $\bar{I}_t$ by approximately 180°. This phase shift can enhance the attenuation of flux density leakage strength. The value of P_k is directly related to the choice of the resonating capacitance in the shielding coil, and even small variations in this parameter can produce large changes in shielding performance;
- Q_k, the quality factor of the k-th resonator, should also be maximized to reduce the power losses and enhance the resonance. A high Q_k requires accurate design of the shielding coils, including material selection, winding geometry, and parasitic loss (R_k) minimization.

A qualitative yet accurate assessment of the proposed shielding concept can be carried out by applying the design criteria discussed above within a quasi-static system model [28,40,41]. However, the presence of ferrite bars in the DWPC setup requires a full-wave numerical analysis of the entire WPT system to identify the most suitable shielding-coil array configuration. To this end, a Finite Element Method (FEM) model was implemented in the commercial software Ansys Maxwell. The numerical solution of the electromagnetic fields was post-processed through two key performance indicators: (a) the average magnetic flux density magnitude evaluated over a target test plane, as defined in (14); and (b) the shielding effectiveness computed on the same plane, as given in (15). The adopted approach relies on a multi-parameter analysis aimed at maximizing leakage-field attenuation, with particular emphasis on the inter-element spacing and on the position of the shielding array relative to the TX and RX coils. The numerical results were finally validated through experimental measurements on the DEXTER platform, as described in Section 7, which are essential for corroborating the proposed design procedure.

$$B_{avg} = \frac{1}{S} \iint_S |B| dS \tag{14}$$

$$K = \frac{\left|B_{avg(with\ coil\ matrix)}\right| - \left|B_{avg(without\ coil\ matrix)}\right|}{\left|B_{avg(without\ coil\ matrix)}\right|} \tag{15}$$

where:

- $B = \left(B_x\hat{x} + B_y\hat{y} + B_z\hat{z}\right)$ is the flux density vector;

- $|B| = \sqrt{B_x^2 + B_y^2 + B_z^2}$ represents the magnitude of the flux density;
- S is the total surface area of the test plane;
- B_{avg} is the average flux density strength over the test plane.

In the following sections, the DEXTER platform is described in detail, together with its application in validating the proposed electromagnetic behavioral models and in supporting the system-level performance characterization of DWBC systems.

3. The DEXTER Prototype

The DEXTER prototype is based on the WDBC series-series compensated reference architecture shown in Figure 1. It was designed to operate at a maximum power level of 300 W and implemented at a 1:2 scale.

The 1:2 geometric scaling factor was selected as a trade-off between laboratory feasibility and electromagnetic representativeness. From a practical standpoint, the reduced scale enables safe operation, manageable thermal conditions, and compatibility with the spatial constraints of a standard university laboratory environment. From a technical perspective, maintaining realistic air-gap proportions, coil aspect ratios, and operating frequency (around 85 kHz) ensures that the fundamental electromagnetic coupling mechanisms, resonance behavior, duty-cycle saturation effects, and shielding phenomena remain physically representative of full-scale Dynamic Wireless Power Transfer systems. Therefore, the adopted scaling preserves the validity of experimental validation of mutual inductance modeling, dynamic performance analysis, and shielding assessment, while enabling cost-effective, reproducible prototyping.

The prototype comprises the following parts:

- two pairs of Transmitter (TX) and Receiver (RX) coils, with different winding configurations and ferrite pad arrangements (Figure 10);
- a 3D motion system capable of moving the RX module, mounted on a trolley with adjustable height and speed, along arbitrary trajectories above the TX coil, within a workspace of 200 cm $\times$ 150 cm (Figure 11);
- a digitally controlled 300 W TX inverter board, enabling the regulation of the TX coil current $I_{1,\mathrm{ref}}$ up to 8 Arms, with an input voltage V_{in} ranging from 12 V to 48 V (Figure 12a);
- a RX-side power conversion board, including a diode bridge rectifier and a digitally controlled 250 W post-regulation DC–DC converter, allowing the RX equivalent load resistance $R_{\mathrm{ac,ref}}$ to be adjusted from 8 Ω to 50 Ω with a battery voltage V_{bat} between 12 V and 48 V (Figure 12b);
- a set of electromagnetic shielding coils and field sensors for electromagnetic exposure assessment (Figure 13). They were designed to achieve the best possible quality factor, aiming to minimize ohmic losses and thus the Joule effect. Specifically, the shielding coils were realized with Litz wires, resulting in a measured Q factor around 40 and a self-resistance of 10 mΩ;
- a MATLAB-based monitoring and control interface, enabling programmable static and dynamic tests for WDBC performance evaluation, as well as Hardware-in-the-Loop (HiL) model validation and refinement (Figure 14);

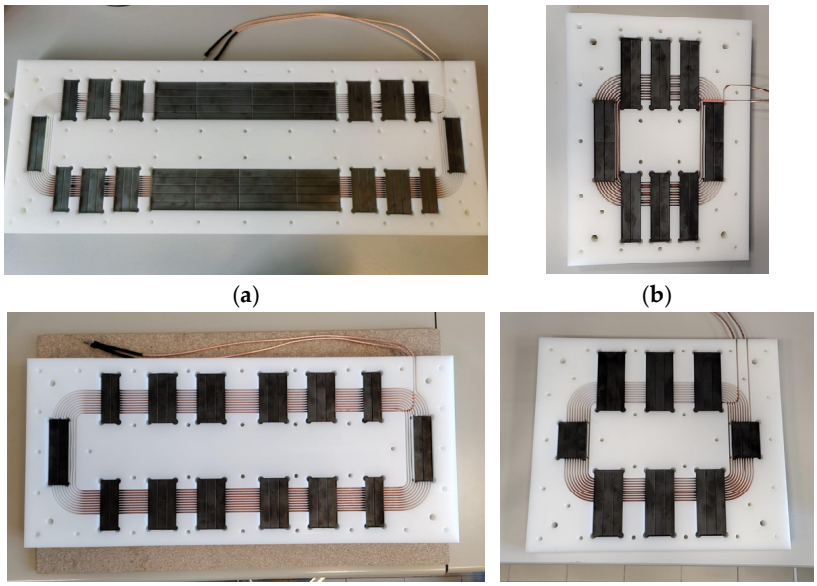

(**a**) (**b**)

(**c**) (**d**)

Figure 10. TX and RX coils used in the DEXTER prototype TX and RX coils: TX coil (**a**,**c**) with the RX coil positioned above it (**b**,**d**), and internal ferrite arrangement of the TX and RX coils.

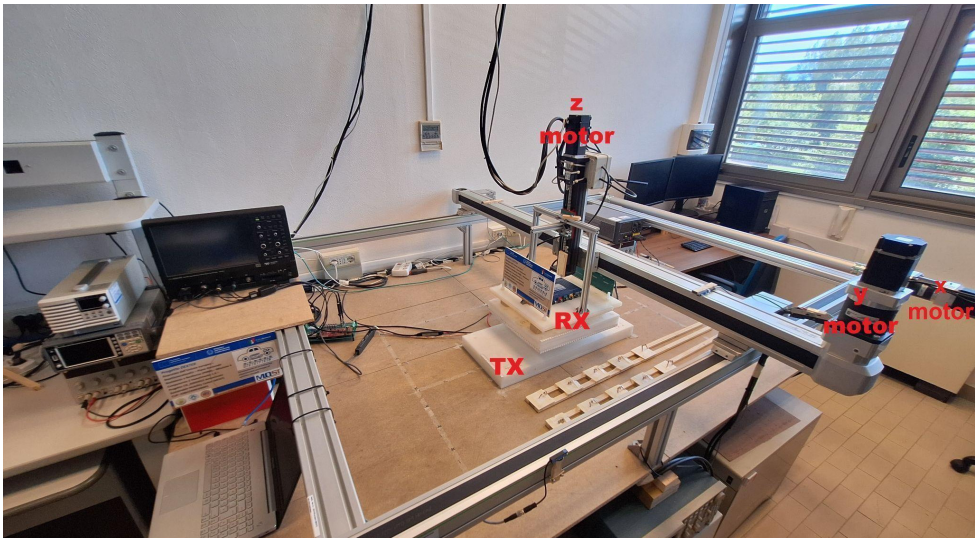

Figure 11. 3D motion system used for dynamic WPT testing. The RX coil is mounted on a motorized trolley with adjustable height and speed, allowing controlled movement along arbitrary trajectories above the TX coil.

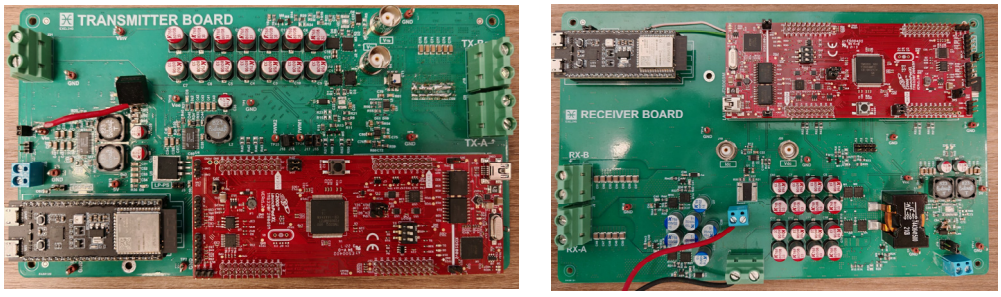

(**a**) (**b**)

Figure 12. (**a**) TX power electronic board; (**b**) RX power electronic board.

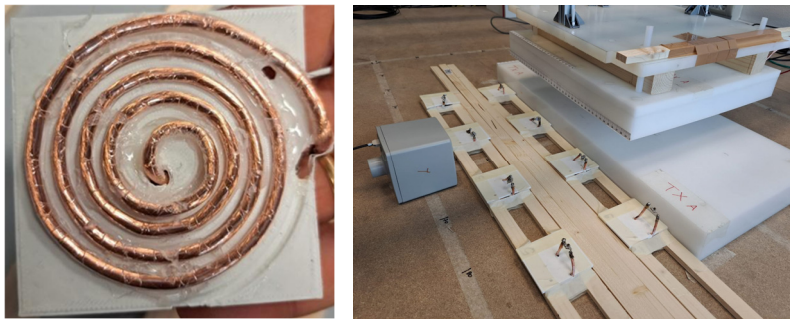

(**a**) (**b**)

Figure 13. Electromagnetic shielding coils and field-measurement setup: (**a**) example of a shielding coil used to mitigate the magnetic field around the WPT link; (**b**) example of a possible measurement setup, with shielding coils placed beside the TX–RX link and a field sensor positioned for magnetic-field assessment.

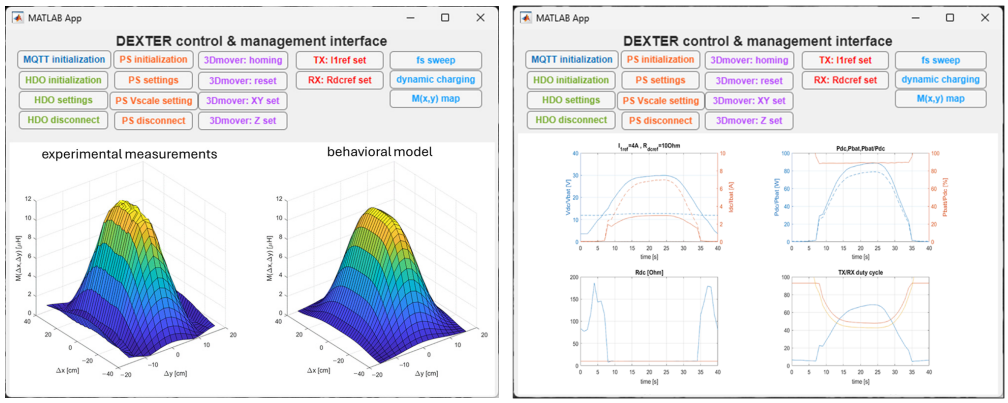

(**a**) (**b**)

Figure 14. MATLAB-based user interface of the DEXTER platform, enabling configuration of test parameters, with (**a**) real-time monitoring of electrical quantities and coil position, and (**b**) automated execution of static and dynamic DWBC experiments.

- a Keysight Technologies E36731A programmable battery emulator with dedicated management software;
- a T3PS30721P DC power supply, rated at 72 A/800 V/720 W;
- a Teledyne LeCroy T3PM1100 digital power meter;
- a Teledyne LeCroy HDO6454 digital oscilloscope;
- a PICOSCOPE 3000 Series USB oscilloscope;
- a Narda EPH200 electromagnetic field probe.

An overview of the entire system is provided in Figure 15, which presents a block diagram summarizing all the components described above. The DEXTER digital architecture is organized into a distributed, low-level, real-time digital control layer and a centralized, high-level setting and monitoring interface layer. The real-time digital control layer is implemented on the TX inverter and RX rectifier/post-regulator boards using two Texas Instruments TMS320F28069M 90 MHz microcontrollers, while configuration and monitoring functions are handled via a MATLAB-based interface running on a laptop. The TX microcontroller implements a PI controller with bandwidth > 10 Hz, whose primary task is to regulate the TX coil RMS current to the reference value $I_{TX,ref}$. The RX microcontroller implements a PI controller with bandwidth > 100 Hz, regulating the input impedance of the RX post-regulator to a reference value $r_{ac,ref}$. The controller bandwidths depend on the TX inverter DC input voltage, the RX battery voltage, and the selected reference pair

$\{I_{TX,ref}, r_{ac,ref}\}$. The worst-case bandwidth supports dynamic tests with RX speeds up to 10 m/s; for safety reasons, laboratory tests were performed at speeds up to 10 cm/s.

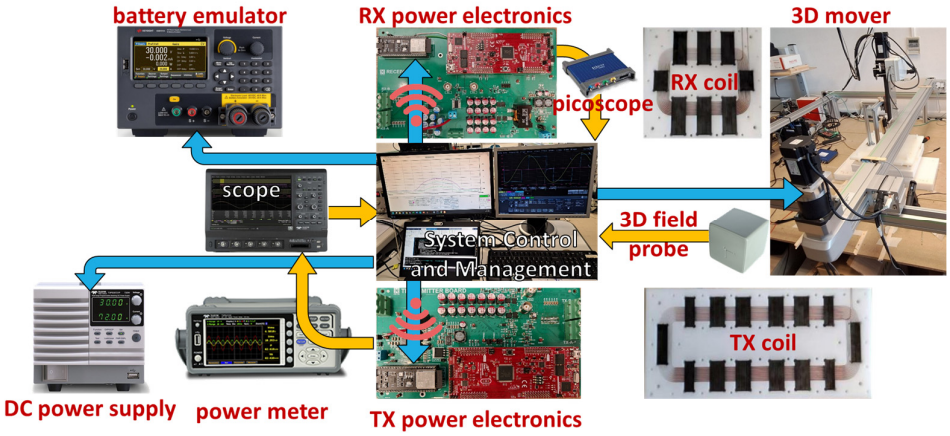

Figure 15. Block diagram of the DEXTER prototype. The figure provides an overview of the complete system architecture, including the TX and RX power stages, the motion platform, the shielding and sensing units, the control and monitoring interfaces, and the measurement equipment.

During dynamic testing, the reference commands $I_{TX,ref}$ and $r_{ac,ref}$ are transmitted to the TX and RX microcontrollers via ESP32-S3-DevKitC-1 Wi-Fi communication boards before the RX motion starts, enabling closed-loop regulation. Since the references remain fixed during each test, the control task does not incur additional latency once motion begins. The TX microcontroller acquires the TX RMS current in real time through one of its 12-bit ADC channels with a sampling frequency equal to one-third of the TX inverter switching frequency, while the RX microcontroller acquires the post-regulator input voltage and current through two 12-bit ADC channels sampled at one-third of the RX post-regulator switching frequency. All digital signals are low-pass filtered with a 1 kHz bandwidth.

The MATLAB interface also manages runtime acquisition of oscilloscope signals from the TX and RX boards at 1 Hz, ensuring reliable sampled data transfer for monitoring. These signals are not used for real-time control, as both microcontrollers independently acquire the required feedback signals through their local ADC channels.

To evaluate the performance of the DEXTER platform under both static and dynamic operating conditions, the system supports a broad set of programmable tests that cover motion control, power electronic regulation, sensing, and EMC-relevant measurements.

The main tests currently implemented to verify the prototype's functionalities are the following:

1. **Static positioning tests**: placing the RX coil at a specified location (X,Y,Z) relative to the TX coil;
2. **Point-to-point motion**: moving the RX coil from an initial position (X_1,Y_1,Z_1) to a final position (X_2,Y_2,Z_2) with predefined acceleration and speed profiles;
3. **Stop-and-go trajectory execution**: driving the RX coil through a sequence of N arbitrary spatial points (X_k,Y_k,Z_k), $k = 1, \ldots, N$, each with configurable acceleration, speed, and dwell time;
4. **TX-side inverter control**: setting the input voltage V_{in}, the switching frequency f_S, and the operating mode of the TX inverter, either (a) open-loop, with a fixed duty cycle DTX, or (b) closed-loop, with regulation of the TX coil RMS current to a reference value $I_{1,ref}$;
5. **TX current verification**: checking the achievement of $I_{1,ref}$ and capturing the corresponding waveform and parameters using the LeCroy HDO6054 oscilloscope;

6. **RX-side converter control**: selecting the operating mode of the RX POST-REG converter, either (a) open-loop, with a fixed duty cycle D_{RX}, or (b) closed-loop, with regulation of the equivalent load resistance to a reference value $R_{ac,ref}$;
7. **RX load verification**: validating the achieved RX load value and acquiring voltage and current waveforms using the PicoScope 3000 Series USB oscilloscope;
8. **Battery emulation**: selecting and configuring the battery model parameters via the Keysight E36731A battery emulator and its management software;
9. **Battery-side signal acquisition**: verifying the emulator operation and measuring voltage and current waveforms using the PicoScope 3000 Series USB oscilloscope;
10. **Magnetic-field measurement**: evaluating the magnetic flux density around the TX coil using the Narda EPH200 field probe and its dedicated software interface;
11. **Resonance frequency mapping**: performing a frequency sweep of the TX coil current over a set of discrete switching frequencies (f_{s1}, …, f_{sN}) at a fixed RMS current reference, using a stop-and-go algorithm along the nominal RX trajectory. For each frequency, the input voltage and current waveforms are captured, the TX inverter duty cycle D_{TX} is computed, and the resonance frequency is identified as the value of f_s for which D_{TX} reaches its minimum;
12. **Mutual inductance mapping**: measuring the TX–RX mutual inductance over a grid of N RX positions (X_k,Y_k) at a fixed height Z, using a stop-and-go algorithm. At each position, the RX open-circuit RMS voltage $V_{2,rms}(X_k,Y_k)$ is acquired with the TX coil driven at the resonance frequency $f$res and at a fixed RMS current $I_{1,ref}$. The mutual inductance is then computed as:

$$M(X_k, Y_k) = \frac{V_{2,rms}(X_k, Y_k)}{2\pi\, f_{res} I_{1,ref}} \tag{16}$$

The procedure may be repeated by changing the vertical distance between coils (height Z), obtaining, in fact, a 3D mapping of the relative positions;
13. **Dynamic performance testing**: recording voltage and current waveforms at the input and output of both the TX power stage and the RX POST-REG converter while the RX coil moves continuously along a linear trajectory from (X_1,Y_1) to (X_2,Y_2) at a fixed height Z. Tests are repeated for different combinations of RX load resistance and TX current reference. Waveforms are captured periodically along the path, with the sampling rate automatically adapted based on the trajectory length and the configured acceleration and speed;
14. **Shielding efficacy**: performing magnetic-field measurements around the WPT link using the Narda EPH200 probe, which, through its dedicated software, allows acquiring the three orthogonal components of the magnetic flux density (B_x, B_y, B_z) along the chosen spatial coordinates (x,y,z).

Beyond the functionalities currently implemented, the modular structure of the DEXTER platform enables the integration of additional tests in the future, including advanced magnetic-field mapping procedures. These extensions will support deeper experimental investigations, particularly those related to human exposure assessment and electromagnetic compatibility, by enabling accurate spatial characterization of the field in realistic dynamic WPT conditions.

Several of the experimental procedures described above are examined in detail in the following sections. In particular, we focus on the last four tests listed previously, namely, the resonance frequency mapping (Test 11, see Section 4), the mutual induction mapping (Test 12, see Section 5), the dynamic performance testing (Test 13, see Section 6) and the magnetic-field measurement (Test 14, see Section 7), as they constitute the core validation

tools of the proposed WPT characterization framework. All tests are carried out using the same reference configuration of the DEXTER prototype, realized with the coil pair shown in Figure 10c,d. Table 1 summarizes the main electrical parameters of the DEXTER prototype used in the experimental validation campaigns presented in Sections 4–7.

Table 1. Main electrical parameters of the DEXTER experimental setup.

Parameter	Symbol	Value	Unit	Notes
TX self-inductance	L_{TX}	108	µH	Measured at nominal configuration
RX self-inductance	L_{RX}	58	µH	Measured at nominal configuration
TX series resistance	R_{TX}	55	mΩ	Including ESR of coil and C_{TX}
RX series resistance	R_{RX}	32	mΩ	Including ESR of coil and C_{RX}
TX compensation capacitor	C_{TX}	33	nF	Selected for nominal resonance
RX compensation capacitor	C_{RX}	60	nF	Selected for nominal resonance
Nominal resonance frequency	f_r	85	kHz	Nominal value
Maximum TX RMS current	$I_{TX,max}$	20	A	Converter limit
RX equivalent load range	R_{ac}	8–50	Ω	Programmable
TX input voltage range	V_{in}	12–48	V	DC input
Maximum output power	P_{max}	300	W	Rated system power
Operating switching frequency	f_s	80–90	kHz	Sweep range

To explicitly address measurement uncertainty and instrument accuracy, Table 2 summarizes the sensing and measurement systems implemented in the DEXTER platform, along with their worst-case accuracy specifications.

Table 2. Accuracy parameters of the DEXTER sensing and measurement system.

Measurement Quantity	Instrument/Sensor	ADC Resolution	Worst Case Accuracy	Notes
Real-time digital-control layer				
TX RMS current (I_{TX})	1/50 current transformer, 10 Ω sensing resistor (±0.1% tol.), peak detector (±3% acc.), 12-bit ADC integrated in the TX TMS320F28069M µC board	~800 µV	±3.1% ± 800 µV	The peak detector includes 6 resistors with ±0.5% tolerance and an active 1 kHz low-pass filter
RX post-regulator input voltage (V_{dc})	Resistive divider (±0.5% tol.), 12-bit ADC integrated in the RX TMS320F28069M µC board	~800 µV	±0.5% ± 800 µV	It includes 2 resistors with ±0.5% tolerance
RX post-regulator input current (I_{dc})	5 mΩ/±0.5% shunt resistor, INA293A3 (±0.15% acc.), Resistive divider (±0.5%/ ±0.1% tol.), 12-bit ADC integrated in the RX TMS320F28069M µC board	~800 µV	±0.8% ± 800 µV	The current monitor includes a 1 kHz low-pass output filter
high-level monitoring interface layer				
TX voltage (V_{TX})	Teledyne LeCroy HDO6454 (500 MHz)	12-bit (~800 µV)	±0.5% FS ±800 µV	±100 mV ± 800 µV at 5 V/div ±200 mV ±800 µV at 10 V/div
TX current (I_{TX})			±0.5% FS ±800 µV	±40 mV ±800 µV at 5 V/div
RX voltages (V_{dc}, V_{batt})	PicoScope 3403D (50 MHz) (on-board moving trolley)	8-bit (~13 mV)	±3% FS ±13 mV	±600 mV ±13 mV at 5 V/div ±1200 mV ±13 mV at 10 V/div
RX current (I_{dc})			±3% FS ±13 mV	±240 mV±13 mV at 2 V/div

4. Resonance Frequency Mapping

This test is essential in practical DWBC systems to evaluate coil tolerances and compensation accuracy, as well as to determine the optimal switching frequency of the TX inverter to achieve optimal operational performance.

Figure 16 illustrates the magnitude of an R–L–C impedance as a function of the operating frequency f, plotted on a double-logarithmic scale. For $f < f_r$, where f_r denotes the resonance frequency, the impedance is dominated by the capacitive term, and its magnitude decreases with a slope of -20 dB/decade. Conversely, for $f > f_r$, the impedance becomes inductive, and its magnitude increases with a slope of +20 dB/decade. At resonance, the impedance magnitude reaches its minimum value, which coincides with the resistance R. The relationship between the voltage and current phasor magnitudes is given by $V(f) = Z(f)I(f)$. Therefore, if the current magnitude is kept constant while its frequency is swept across the resonance frequency f_r, the resulting voltage magnitude follows the impedance profile and achieves its minimum at resonance. Accordingly, the resonance frequency of the TX coil has been identified by performing test 11 on the DEXTER platform, with the RX coil kept open-circuited while the TX inverter (TX INV) regulates the TX coil current to a fixed reference value $I_{\mathrm{TX,ref}}$. During this procedure, the switching frequency is swept over a range $[f_{s,\min}, f_{s,\max}]$ centered around the nominal resonance frequency of 85 kHz. Under these conditions, the TX inverter effectively drives an impedance composed of the series combination of R_{TX}, L_{TX}, and C_{TX}.

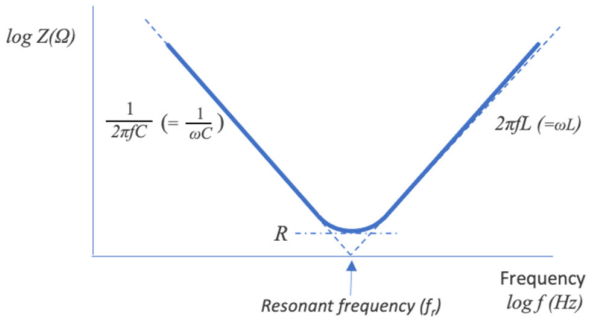

Figure 16. Resonance frequency of a series R-L-C impedance.

Figure 17 shows the voltage and current waveforms of both the TX and RX coils at different switching frequencies f_s, obtained during the sweep while regulating the TX coil current to a constant value. In Figure 17a, the sinusoidal TX current leads the square-wave TX voltage, a condition occurring when $f_s < f_r$, indicating a capacitive behavior dominated by C_{TX}. In Figure 17c, the current lags behind the voltage, as expected when $f_s > f_r$ and the behavior becomes inductive, dominated by L_{TX}. In Figure 17b, the voltage and current waveforms are nearly in phase, indicating operation close to the resonance frequency f_r, where the circuit behaves predominantly as a resistance governed by R_{TX}.

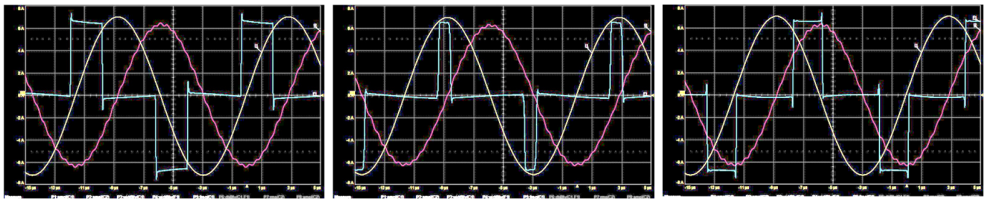

(**a**) (**b**) (**c**)

Figure 17. Voltage and current waveforms of the TX and RX coils with the RX coil open-circuited, captured at different switching frequencies: (**a**) $f_s < f_r$; (**b**) $f_s = f_r$; and (**c**) $f_s > f_r$. Cyan = TX voltage, yellow = TX current, magenta = RX voltage.

Moreover, the TX voltage waveform exhibits a minimum value of the on-time $t_{TX,on}$ when f_s is close to f_r. This behavior arises from the relationship between the voltage first harmonic $V_{TX}(f_s)$ generated by the TX inverter and the on-time of the applied square wave:

$$V_{TX}(f_s) = \frac{4}{\pi} sin(f_s t_{TX,on}) \quad (17)$$

Consequently, the resonance frequency can be detected by executing an automatic stop-and-go frequency sweep while regulating the TX coil current to a constant value and monitoring the on-time of the TX voltage. The resonance frequency corresponds to the switching frequency at which $t_{TX,on}$ reaches its minimum.

Test 11 was carried out with the RX coil open-circuited and positioned 10 cm above the TX coil, considering two different (x,y) locations relative to the TX coil: (a) far from the TX coil ($x = -60$ cm, $y = -40$ cm), and (b) centered above it ($x = 0, y = 0$). During the test, the TX coil was driven by the TX INV converter with V_{in} = 18 V, $I_{TX,ref}$ = 5 A, and a switching-frequency sweep over the range [84 kHz, 89 kHz]. The TX coil was compensated using capacitors selected according to the expected resonance frequency and the nominal stand-alone self-inductance LTX. Figure 18 reports the measured values of the duty cycle DTX required by the TX INV to regulate the TX current to 5 A for the two RX coil positions (a) and (b). As previously discussed, the resonance frequency corresponds to the switching frequency that minimizes the duty cycle. The resulting resonance frequencies are approximately 86.5 kHz when the RX and TX coils are aligned and 87 kHz when the TX coil operates alone, neither of which matches the nominal 85 kHz value.

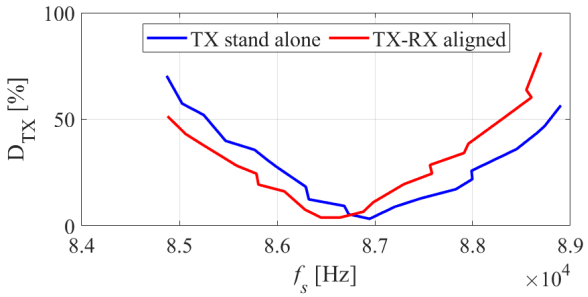

Figure 18. Duty cycle DTX set by the TX INV converter to regulate the TX coil current to 5 A, measured during the switching-frequency sweep for the two RX coil positions considered in Test 11.

5. Mutual Inductance Mapping

This test is crucial in DWBC systems for comprehensive characterization of the spatial variation in the mutual inductance between the TX and RX coils, especially under misalignment and trajectory-dependent operating conditions. This test also indirectly demonstrates that the DEXTER platform can function as an effective generator of experimental datasets, enabling the derivation of behavioral models directly from measurements rather than relying solely on simulated data [21]. This capability is particularly valuable for capturing real-world effects, including nonidealities, construction tolerances, and magnetic-core imperfections, that may not be fully represented in full numerical models.

Measurement campaigns were performed by executing Test 12 with the DEXTER platform, operating the coils directly within the WPT prototype and controlling the procedure via the integrated MATLAB interface. The experimental mapping was conducted over a 3D grid of N = 697 RX coil positions, obtained by combining 41 values of longitudinal displacement Δx (from –40 cm to +40 cm, in 2 cm steps) and 17 values of lateral displacement Δy (from –16 cm to +16 cm, in 2 cm steps), for two vertical distances between the coil planes: Δz = 7.5 cm and Δz = 10 cm. At each grid point (X_k,Y_k), the TX coil was driven at

the resonance frequency f_r identified from Test 11, with the TX coil RMS current regulated to a fixed value $I_{1,\mathrm{ref}}$ = 3 A. The TX inverter input voltage was set to V_{in} = 5 V. The RX coil was left open-circuited, and the induced RMS voltage $V_{2,\mathrm{rms}}(X_k,Y_k)$ was measured using the LeCroy HDO6454 oscilloscope. The mutual inductance at each position was then calculated using (16), which derives directly from the definition of the open-circuit induced voltage in the secondary coil of a transformer excited by a sinusoidal primary current. It is worth noting that the experimental estimate in (16) is in good agreement with the mutual inductance computed using a full 3D electromagnetic model implemented in Ansys.

Figure 19a,b compare the mutual inductance maps obtained experimentally with those predicted by the behavioral model in (6) and (7). The close correspondence between the two confirms not only the accuracy of the adopted model but also the capability of the DEXTER platform to generate precise, repeatable datasets suitable for behavioral model identification and refinement.

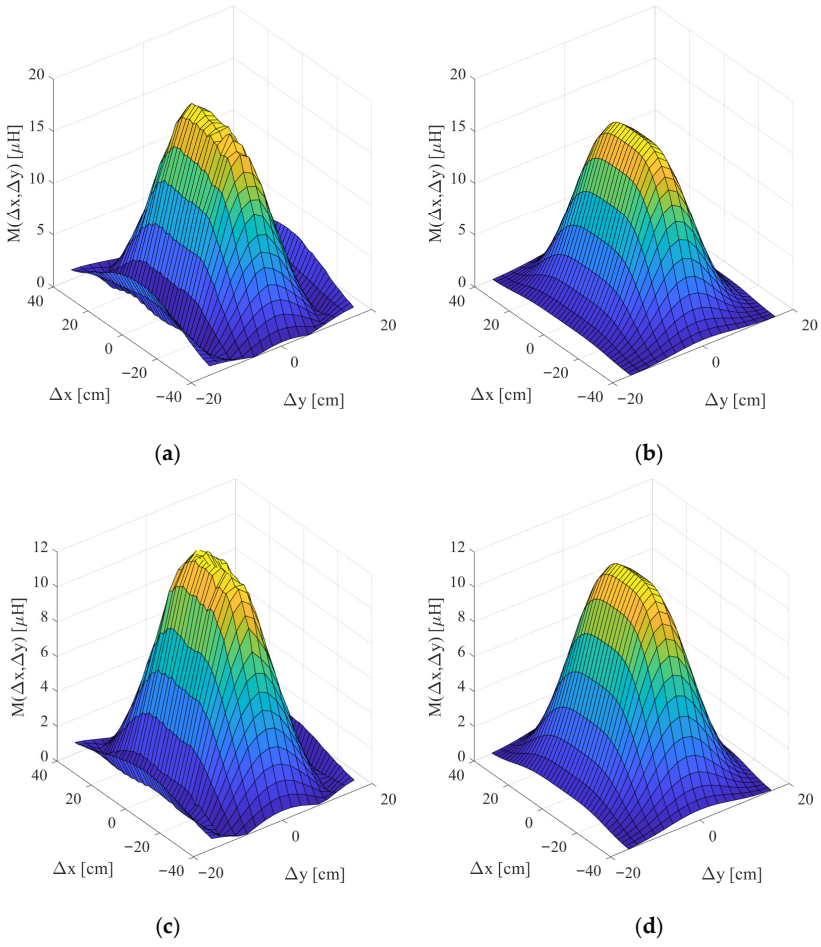

Figure 19. TX-RX mutual inductance surface plots for (**a**) Δz = 7.5 cm and (**b**) Δz = 10 cm: DEXTER experimental measurements on the left, behavioral model results on the right. TX–RX mutual inductance surface plots for (**a**) Δz = 7.5 cm and (**c**) Δz = 10 cm: DEXTER experimental measurements (**left**) and behavioral model predictions (**right**), corresponding respectively to subfigures (**b**,**d**).

6. Dynamic System Performance Testing

Dynamic performance testing plays a crucial role in assessing the real operating behavior of a WPT system. Unlike static characterization, dynamic tests enable the evaluation of how the converter control loops, resonant behavior, and power-transfer capability respond to time-varying coupling conditions induced by motion. Test 13, therefore, provides a comprehensive end-to-end validation of the mathematical model presented in Section 2.1,

confirming its ability to predict system behavior under realistic operating conditions. Furthermore, this test enables verification of the interaction between the TX inverter, the RX post-regulator, and the battery load during continuous coil motion, thereby assessing overall system stability, efficiency, and power-handling capability.

Test 13 was executed by programming a linear trajectory of the RX coil with the following motion and system settings:

- RX motion along the x-axis, from an initial displacement of $x = -40$ cm to a final displacement of $x = +40$ cm relative to the TX coil;
- constant motion speed: 2 cm/s;
- fixed lateral displacement: $y = 0$ cm;
- fixed vertical displacement: $z = 10$ cm;
- TX inverter input voltage: $V_{in} = 18$ V;
- TX coil current reference: $I_{TX,ref} = 5.6$ A;
- RX DC load reference values: $R_{dc,ref} = \{10, 20\}$ Ω, equivalent to $R_{ac,ref} = \{8.1, 16.2\}$ Ω;
- battery model: 12 V, 7.35 Ah.

During the RX motion along the programmed trajectory, the following quantities were recorded:

- input voltage V_{dc} and input current I_{dc} of the RX DC-DC post-regulator operating in buck mode;
- battery voltage Vbat and battery current Ibat at the output of the RX post-regulator;
- effective DC input resistance of the RX regulator $R_{dc} = V_{dc}/I_{dc}$;
- duty cycle D_{TX} of the square-wave output voltage of the TX inverter;
- duty cycle D_{RX} of the RX post-regulator in buck mode.

Figure 20 reports the results of Test 13 for the case $R_{dc,ref} = 10\,\Omega$ ($R_{ac,ref} = 8.1\,\Omega$ and $r_{ac,ref} = 253$). The horizontal time axis spans from 0 s to 40 s, corresponding to the spatial range from −40 cm to +40 cm given the constant speed of 2 cm/s, according to the law $x(t) = -40 + 2\,t$, with x in cm and t in seconds. As shown in Figure 20a,c, the RX DC–DC post-regulator begins regulating the input resistance R_{dc} as soon as the input voltage V_{dc} rises sufficiently above the battery voltage V_{bat}, enabling operation in buck mode ($V_{bat} < V_{dc}$). This transition occurs when the RX coil reaches positions where the mutual inductance $M(x)$ exceeds the threshold required to induce an adequate voltage on the RX side. Once this condition is met, R_{dc} is driven toward its reference value $R_{dc,ref} = 10\,\Omega$, maintaining closed-loop regulation throughout most of the coil transit.

The waveform of Figure 20d shows that, in the central region of the trajectory (when the RX coil is aligned with the TX coil), the duty cycle of the TX inverter reaches its maximum value ($D_{TX} = 100\%$). This saturation limits the inverter's ability to maintain the reference TX current, leading to a slight de-rating of the TX coil current amplitude with respect to $I_{TX,ref}$. The saturation of D_{TX} also forces the RX-side duty cycle D_{RX} to increase, as seen in Figure 20d, to compensate for the reduced transmitted power. The corresponding reduction in both the DC input power P_{dc} and the battery charging power P_{bat} is visible in Figure 20b, where the efficiency of the RX DC–DC converter is also plotted along the trajectory.

Similarly, Figure 21 presents the results of Test 13 for the case $R_{dc,ref} = 20\,\Omega$ ($R_{ac,ref} = 16.2\,\Omega$ and $r_{ac,ref} = 506$). As expected, the general behavior is similar, but with key differences attributable to the lighter RX-side load. Figure 21c confirms that the RX post-regulator can still maintain an extended regulation interval of R_{dc}, since V_{dc} again exceeds the battery voltage early enough along the trajectory due to the given TX current reference. However, Figure 21d shows that the TX inverter duty cycle does not reach saturation in this case: the reduced load demand requires a smaller D_{TX} to sustain the target TX current, avoiding

the clipping observed with $R_{dc,ref}$ = 10 Ω. Finally, Figure 21c also shows that both P_{dc} and P_{bat} reach lower peak values than in Figure 20. This is consistent with the higher RX-side impedance, which results in reduced energy transfer despite stable regulation conditions.

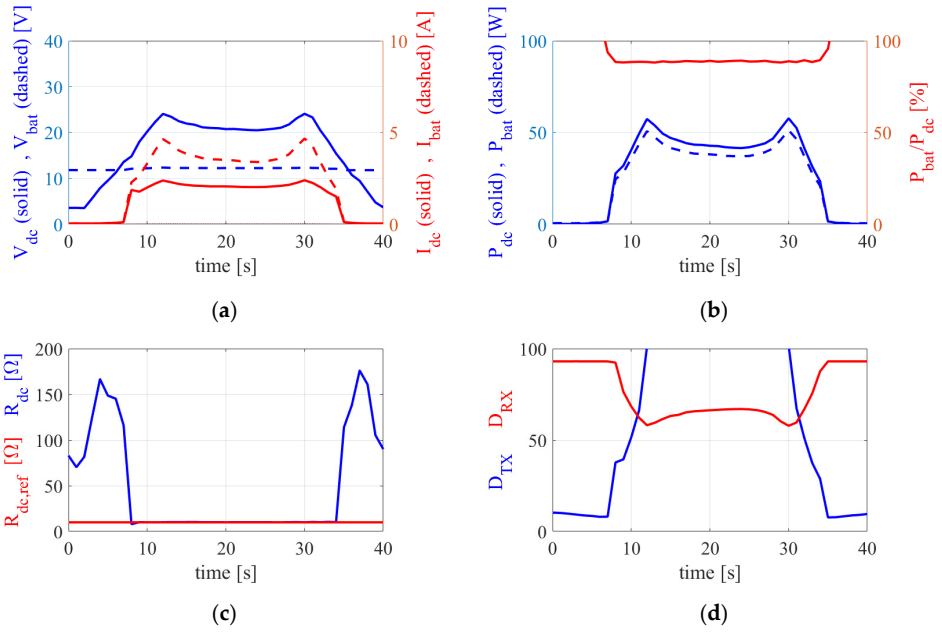

Figure 20. Results of Test 13 with $I_{TX,ref}$ = 5.6 A, $R_{dc,ref}$ = 10 Ω ($R_{ac,ref}$ = 8.1 Ω, $r_{ac,ref}$ = 253). Rectifier output and battery (**a**) voltages and currents and (**b**) power and battery efficiency; (**c**) estimated DC resistance and its reference; (**d**) TX and RX duty cycles.

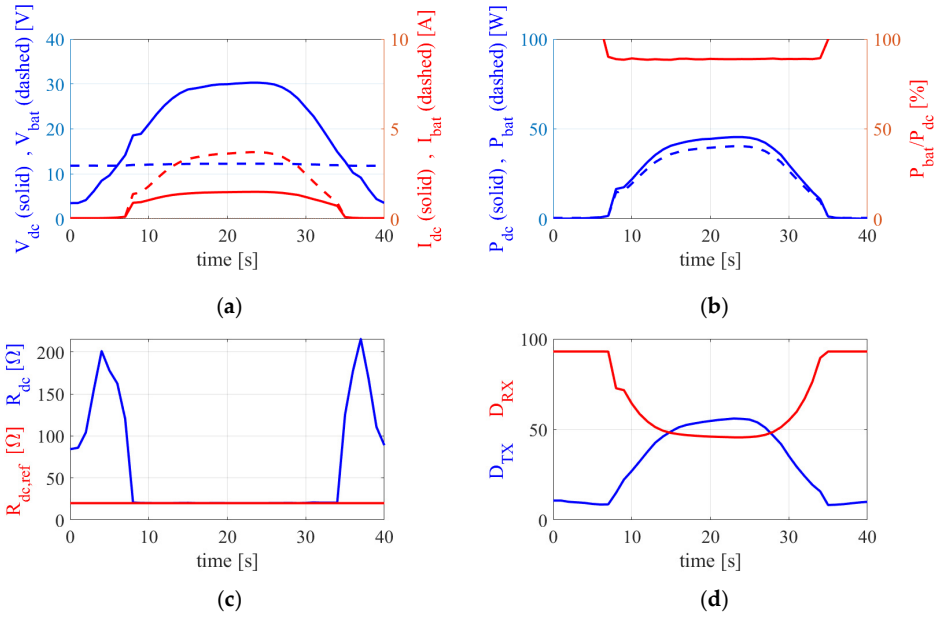

Figure 21. Results of Test 13 with $I_{TX,ref}$ = 5.6 A, $R_{dc,ref}$ = 20 Ω ($R_{ac,ref}$ = 16.2 Ω, $r_{ac,ref}$ = 506). Rectifier output and battery (**a**) voltages and currents and (**b**) power and battery efficiency; (**c**) estimated DC resistance and its reference; (**d**) TX and RX duty cycles.

7. Shielding Efficiency

Based on the design guidelines described in Section 2.3, the final shielding configuration consists of 10 resonant coils per side. On each side, the coils are arranged into two adjacent sub-arrays of 5 elements, forming a 2 × 5 matrix, as shown in Figure 22. Owing to the symmetry of the system and considering that the reaction field generated by the shield

located on the opposite side of the TX–RX coils is negligible with respect to the source field produced by the TX–RX pair, only one side of the setup was equipped with the shielding array in order to simplify the experimental arrangement and the measurements.

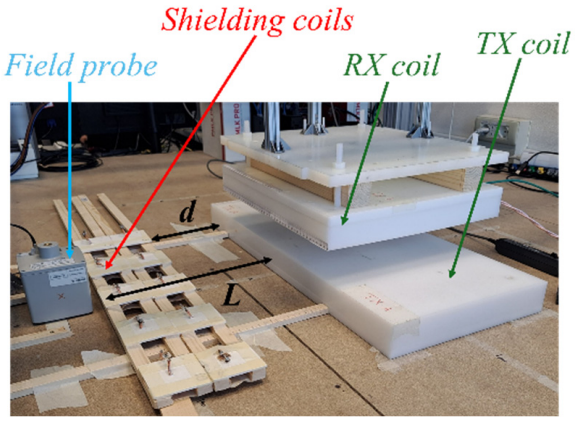

Figure 22. Measurement setup of Test 14: the flux density probe is positioned at a distance L = 41.5 cm from the TX coil. The TX and RX coils are placed in a centered configuration. The 2 × 5 shielding coil array is placed at a variable distance d from the TX coil.

The 2 × 5 array was positioned at a variable distance d from the TX coil, which was the only parameter swept during the analysis. The inter-element spacings d_x and d_y were kept constant, as determined through a preliminary optimization. The experimental setup and the main geometric parameters are summarized in Figure 23, including d_x and d_y, the distance between the shielding array and the TX coil (d), and the distance between the observation plane and the TX coil (L).

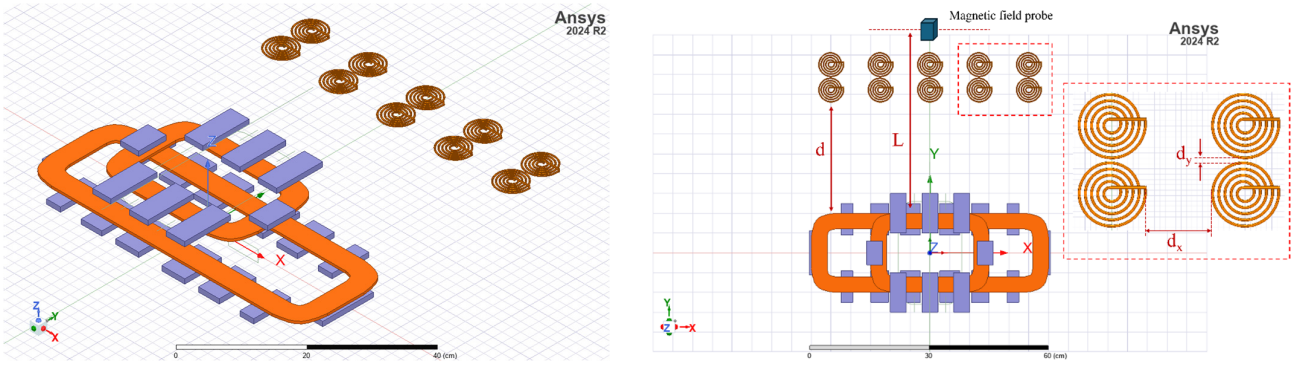

(**a**) (**b**)

Figure 23. (**a**) Overview of the 2 × 5 array configuration inside the WPT system. (**b**) Ansys CAD dimensions description: inter-elements spacing along X axis (d_x) and Y axis (d_y) respectively, distance between the shielding array and TX coil (d), distance between the observation plane and TX coil (L).

The symmetry of the configuration suggests a symmetric magnetic flux-density distribution on the ZX plane, which was confirmed by FEM simulations performed with the complete 3D Ansys Maxwell model of the WPT system, including the integrated 2 × 5 shielding array, as shown in Figure 24. The simulated field map was also used to select the probe location at the point of maximum flux density on the observation plane, constrained by the DEXTER platform's clearance constraints.

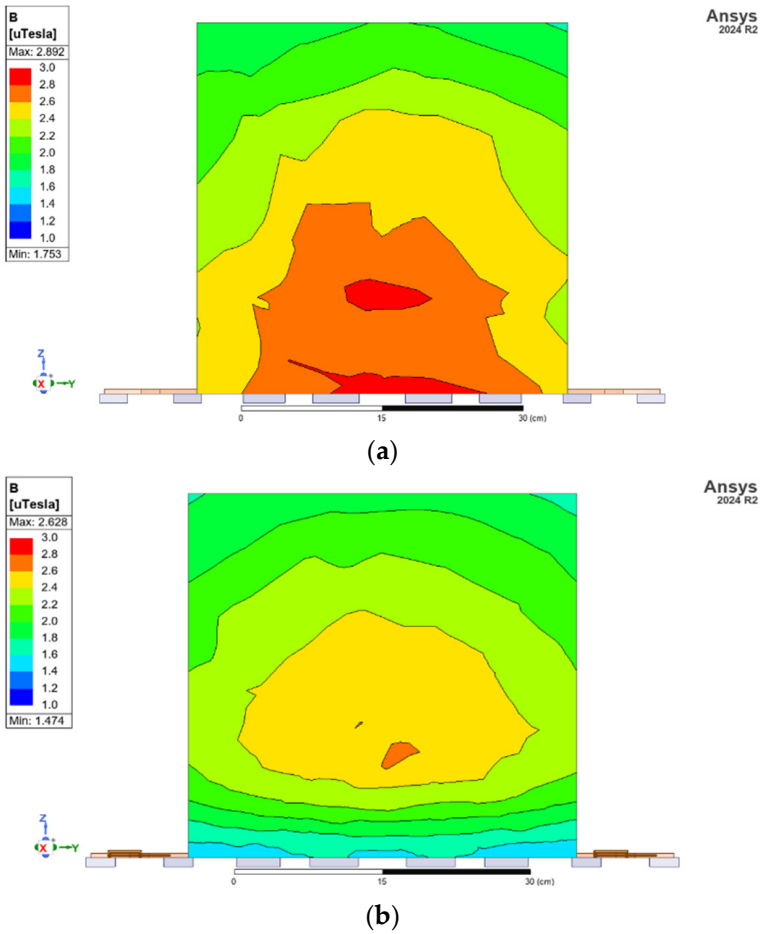

Figure 24. Magnetic flux-density distribution |B| on the observation plane located at L = 41.5 cm from the TX coil, for the 1:2-scale DEXTER prototype operating at f_r = 83.4 kHz, I_{TX} = 5 Arms, R_{ac} = 40 Ω, Δz = 7.5 cm, and zero lateral misalignment (y = 0): (**a**) unshielded configuration; (**b**) configuration with 2 × 5 resonant shielding-coil array placed at d = 23 cm from the TX coil.

Test 14 was carried out by keeping the RX coil fixed and applying the following operating conditions:

- shielding-array displacement along the *y*-axis: *d* swept from 5 cm to 23 cm with respect to the TX coil;
- RX vertical offset: z = 7.5 cm;
- TX coil current reference: I_{TX} = 5 A_{rms};
- RX load: R_{ac} = 40 Ω;
- inter-elements spacing along *x*-axis: d_x = 6.3 cm;
- inter-elements spacing along *y*-axis: d_y = 2 mm;
- magnetic field probe distance from the TX coil: L = 41.5 cm;
- resonance frequency f_r = 83.4 kHz.

The *x*-, *y*- and *z*-components of the magnetic flux density at the probe location were recorded for each shielding-array position. The array position was swept along the *y*-axis by varying the distance *d* from 5 cm to 23 cm in 1 cm increments. The resulting flux-density amplitude $|B|$, plotted as a function of *d* and compared for the cases with and without the shielding coils, is shown in Figure 25 for both measurements and FEM simulations.

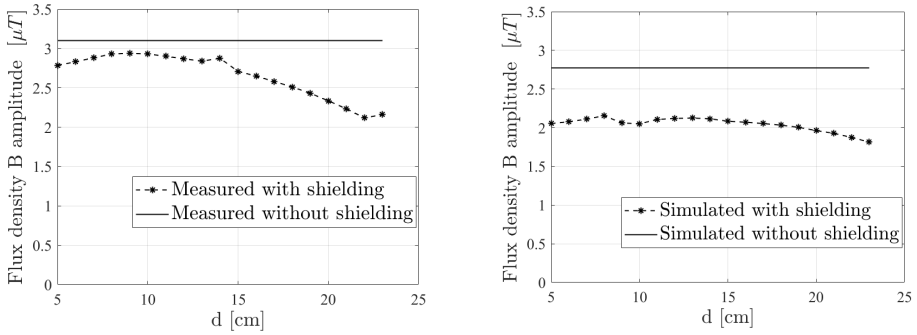

(**a**) (**b**)

Figure 25. Flux density B amplitude plotted by changing the distance d for the setup described in Figure 23 with and without the presence of the shielding coils: (**a**) measurements; (**b**) simulations.

For clarity, the corresponding normalized trend of the flux-density amplitude $|B|$ in the shielded configuration, as a function of d, is reported in Figure 26, where measurements are directly compared with FEM simulation results for the setup described in Figure 23.

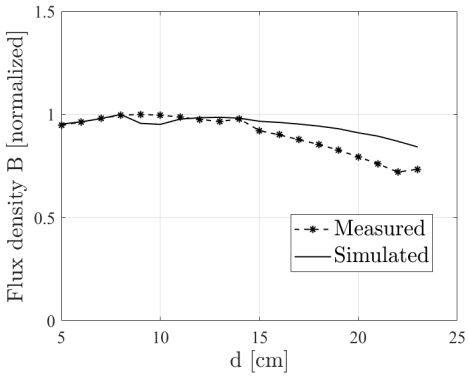

Figure 26. Normalized behavior of flux density B amplitude with the presence of shielding coils plotted by changing the distance d for the setup described in Figure 23. Comparisons between measurements and simulations.

By observing Figures 24 and 26, the following observations can be drawn:

- Both measurements and simulations confirm that the proposed shielding-coil array, in the considered position and configuration, reduces the magnetic flux-density amplitude over the entire investigated range of distances.
- The FEM simulations indicate an almost distance-independent shielding behavior, showing a nearly constant attenuation as the array-to-TX distance varies. However, the experimental results show stronger attenuation at greater distances from the TX coil, suggesting a distance-dependent effect in the measured setup. The slight differences are likely due to uncertainties in the manufacturing process. However, where the difference is present, the real-world shielding coils exhibit better shielding performance than simulations, suggesting that the design method remains reliable. The maximum shielding effectiveness obtained experimentally occurs at d = 22 cm, corresponding to K = 31.48%. The numerical simulations predict the optimal performance at d = 23 cm, with K = 34.68%, indicating good agreement between experimental and simulated outcomes.

Overall, the experimental campaign confirms the proposed design procedure. Nevertheless, the performance of resonant shielding arrays is highly sensitive to fabrication tolerances; therefore, accurate coil winding and tight capacitor tolerances are required to ensure consistent tuning and repeatable shielding performance.

From a safety perspective, the measured magnetic flux density levels can be directly compared with international exposure guidelines. In the unshielded configuration, the measured magnetic field at 25 cm from the WPT system is approximately 3 μT, which is below the first public exposure limit of 6.25 μT specified by the ICNIRP guidelines at the prototype's operating frequency. The introduction of the resonant shielding array results in approximately 31% attenuation at the same distance, further increasing the safety margin. Since the leakage field rapidly decays with increasing distance from the transmitting and receiving coils, the most critical exposure region is near the vehicle. In this area (where passengers, drivers, or nearby pedestrians may be present), the reduction in magnetic flux density achieved by the proposed shielding solution helps improve compliance with international safety recommendations.

8. Conclusions and Future Directions

This paper presents a comprehensive theoretical and experimental investigation of Dynamic Wireless Battery Charging (DWBC) systems, addressing design, control, electromagnetic, and safety aspects at both component and system levels. Specifically, the analysis highlighted how coil geometry, power-electronics regulation, and electromagnetic shielding jointly influence both the energy-transfer performance and electromagnetic safety of dynamic wireless charging infrastructures.

To support the design and optimization of such systems, the DEXTER platform, a 1:2-scale open and modular experimental prototype developed within the POC-MOST project, was introduced. The platform integrates a three-axis motion system, digitally controlled TX/RX power converters, a programmable battery emulator, and a dedicated shielding and field-measurement setup, all coordinated through a MATLAB-based interface enabling automated testing and Hardware-in-the-Loop (HiL) integration. This platform enables reproducible, systematic experimentation under realistic, dynamic operating conditions.

Experimental campaigns demonstrated DEXTER's capability to validate key DWBC models and behaviors, including resonance frequency identification, spatial mutual inductance mapping, and end-to-end dynamic charging performance along controlled trajectories. The results confirmed the accuracy of behavioral electromagnetic models and revealed the impact of converter duty-cycle saturation on power regulation during motion. Furthermore, shielding measurements, supported by FEM simulations, verified the effectiveness of resonant coil-array shielding solutions and highlighted their sensitivity to manufacturing tolerances and tuning accuracy. Since industrialization efforts aim to design solutions that are easy to replicate and manufacture, thereby minimizing fabrication uncertainties, a PCB-based implementation of the shielding coils could offer improved reproducibility in future developments. Another advantage of the PCB version is reduced material dispersion and potential weight optimization. However, achieving comparable electrical performance in terms of quality factor may result in a significant increase in manufacturing costs compared to the current Litz-wire implementation, which serves as a cost-effective proof-of-concept solution.

Beyond serving as a validation tool, the DEXTER platform represents a unified research environment for co-designing power electronics, magnetic structures, and shielding solutions for dynamic wireless charging systems. By enabling integrated performance, EMC, and exposure assessments, it contributes to the development of safer, more efficient, and more sustainable e-mobility infrastructures. Furthermore, the DEXTER platform provides a flexible experimental platform for future quantitative sustainability assessments, enabling systematic comparisons of alternative coil designs, converter architectures, and control strategies in terms of efficiency, material use, and potential impacts on battery downsizing.

In line with the adopted 1:2 geometric scaling, the current DEXTER implementation is limited to 300 W and is intended for model validation and system-level experimentation rather than direct kW-scale operation. One aspect that falls outside the present scope of DEXTER concerns the power converter architecture and the specific technologies adopted for power MOSFETs and passive components in the TX inverter and RX rectifier/post-regulator, along with all related design considerations. Scaling the platform to higher power levels would require a dedicated redesign of the power stages, including selecting appropriately rated components, enhancing thermal management of power MOSFETs and magnetic and shielding elements, increasing conductor cross-sections to limit ohmic losses, and reinforcing structural management. Future developments will focus on: (*i*) extending the platform toward higher power levels and more complex dynamic scenarios, including adaptive and predictive control strategies robust to misalignment and trajectory uncertainties; (*ii*) implementing automated co-design workflows for shielding arrays under realistic manufacturing constraints; and (*iii*) performing systematic EMC and electromagnetic-field exposure assessments in compliance with evolving international standards.

Author Contributions: Conceptualization, G.D.C. and N.F. (Nicola Femia); Data curation, G.D.C.; Formal analysis, G.D.C., N.F. (Nicola Femia), A.M., S.B. and N.F. (Nunzia Fontana); Funding acquisition, G.D.C., N.F. (Nicola Femia) and N.F. (Nunzia Fontana); Investigation, G.D.C., N.F. (Nicola Femia), A.M., S.B. and N.F. (Nunzia Fontana); Methodology, G.D.C., N.F. (Nicola Femia), A.M., S.B. and N.F. (Nunzia Fontana); Project administration, G.D.C., N.F. (Nicola Femia) and N.F. (Nunzia Fontana); Resources, G.D.C. and N.F. (Nicola Femia); Software, G.D.C., N.F. (Nicola Femia) and N.F. (Nunzia Fontana); Supervision, G.D.C. and N.F. (Nunzia Fontana); Validation, G.D.C., N.F. (Nicola Femia) and N.F. (Nunzia Fontana); Visualization, G.D.C., N.F. (Nicola Femia) and N.F. (Nunzia Fontana); Writing—original draft, G.D.C., N.F. (Nicola Femia) and N.F. (Nunzia Fontana); Writing—review & editing, G.D.C., A.M. and S.B. All authors have read and agreed to the published version of the manuscript.

Funding: This study was carried out within the project DEXTER "Development of an Enhanced eXperimental proTotype of wirEless chargeR" in the frame of the PoC call 2nd edition by MOST—Sustainable Mobility Center and received funding from the European Union Next-GenerationEU (PIANO NAZIONALE DI RIPRESA E RESILIENZA (PNRR)—MISSIONE 4 COMPONENTE 2, INVESTIMENTO 1.4—D.D. 1033 17/06/2022, CN00000023). This manuscript reflects only the authors' views and opinions; neither the European Union nor the European Commission can be considered responsible for them. This work was also carried out within the projects "300638FRB24FEMIA—Characterization of Power Components" and "300638FRB25FEMIA—Wireless Power Transfer Systems" funded by the University of Salerno.

Data Availability Statement: The data presented in this study are available on request from the corresponding author, in accordance with the scope of the intended use.

Acknowledgments: The Authors acknowledge the support of EXELING S.r.l. in the design and manufacturing of the TX and RX power electronic converters of the DEXTER prototype, and in the setup of experimental tests. The Authors also acknowledge Gennaro Di Mambro and the CREATE Consortium for their support in the electromagnetic simulation.

Conflicts of Interest: The authors declare that they have no conflicts of interest.

References

1. Patil, D.; McDonough, M.K.; Miller, J.M.; Fahimi, B.; Balsara, P.T. Wireless power transfer for vehicular applications: Overview and challenges. *IEEE Trans. Transp. Electrif.* **2018**, *4*, 3–37. [CrossRef]
2. Iqbal, S.; Alshammari, N.F.; Shouran, M.; Massoud, J. Smart and Sustainable Wireless Electric Vehicle Charging Strategy with Renewable Energy and Internet of Things Integration. *Sustainability* **2024**, *16*, 2487. [CrossRef]
3. Jia, C.; Liu, W.; Chau, K.T.; He, H.; Zhou, J.; Niu, S. Passenger-aware reinforcement learning for efficient and robust energy management of fuel cell buses. *eTransportation* **2026**, *27*, 100537. [CrossRef]

4. Laporte, S.; Coquery, G.; Deniau, V.; De Bernardinis, A.; Hautière, N. Dynamic Wireless Power Transfer Charging Infrastructure for Future EVs: From Experimental Track to Real Circulated Roads Demonstrations. *World Electr. Veh. J.* **2019**, *10*, 84. [CrossRef]
5. Bozhi; Mohamed, M.; Gilani, V.N.M.; Amjad, A.; Majid, M.S.; Yahya, K.; Salem, M. A Review of Wireless Pavement System Based on the Inductive Power Transfer in Electric Vehicles. *Sustainability* **2023**, *15*, 14893. [CrossRef]
6. Ruffo, R.; Cirimele, V.; Diana, M.; Khalilian, M.; Ganga, A.L.; Guglielmi, P. Sensorless Control of the Charging Process of a Dynamic Inductive Power Transfer System with an Interleaved Nine-Phase Boost Converter. *IEEE Trans. Ind. Electron.* **2018**, *65*, 7630–7639. [CrossRef]
7. Abuajwa, O.; Thiagarajah, S.P.; Ambak, Z.; Sarker, T.; Ramasamy, G.; David, A.P. Comprehensive review of wireless power transfer systems for electric vehicle charging applications. *Discov. Appl. Sci.* **2025**, *7*, 1176. [CrossRef]
8. Alotaibi, F.M. Optimized Coupling Coil Geometry for High Wireless Power Transfer Efficiency in Mobile Devices. *J. Low Power Electron. Appl.* **2025**, *15*, 36. [CrossRef]
9. Zhang, J.; Kong, L.; Wang, Z.; Wang, Y.; Liu, Y.; Gao, X.; Zhu, C. Receiver-Side Topologies for Wireless Power Transfer Systems: A Comprehensive Review of the Design, Challenges, and Future Trends. *Energies* **2025**, *18*, 1493. [CrossRef]
10. Yang, L.; Dong, K.; Wang, Y.; Cai, C. Analysis and Design of a Dual-Receiver WPT System with Constant Current and Constant Voltage Dual-Type Outputs. *IEEE Trans. Transp. Electrif.* **2025**, *11*, 4060–4069. [CrossRef]
11. Lee, S.; Cheon, J.; Park, H.; Kim, D. Determination and analysis of compensation capacitor for a robust distance-variable wireless power transfer system. *AIP Adv.* **2024**, *14*, 115220. [CrossRef]
12. Li, X.; Wang, C.; Wang, H.; Dai, X.; Sun, Y.; Hu, A.P. A Robust Wireless Power Transfer System with Self-Alignment Capability and Controllable Output Current for Automatic-Guided Vehicles. *IEEE Trans. Power Electron.* **2023**, *38*, 11898–11906. [CrossRef]
13. Li, Y.; Sun, P.; Liang, Y.; Wu, X.; Sun, J.; Rong, E.; Liu, Y.; Deng, Q. Research on Rectifier Fault Diagnosis and Self-Protecting for Inductive Power Transfer System with Constant-Current Output. *IEEE Trans. Power Electron.* **2025**, *40*, 3750–3769. [CrossRef]
14. Zimmer, S.; Helwig, M.; Winkler, A.; Modler, N. One-way vs. two-way coupled simulation: Investigation of thermal management of wireless power transfer modules for electric vehicles. In Proceedings of the 2022 Wireless Power Week (WPW), Bordeaux, France, 5–8 July 2022. [CrossRef]
15. Panchal, C.; Stegen, S.; Lu, J. Review of static and dynamic wireless electric vehicle charging system. *Eng. Sci. Technol. Int. J.* **2018**, *21*, 922–937. [CrossRef]
16. Yadav, A.; Kanti Bera, T. A critical review of electromagnetic coil assembly design and optimization for wireless power transfer in electric vehicles: Technical insights. *Renew. Sustain. Energy Rev.* **2025**, *223*, 115944. [CrossRef]
17. The DEXTER Project, Italian PNRR Program CN-00000023, PoC 2nd Edition, MOST. Available online: https://www.unicas.it/most/spoke-13-unicas-tasks/progetti-closed-call/ (accessed on 18 March 2026).
18. Di Mambro, G.; Antonini, R.; Oliva, N.; De Guglielmo, L.; Di Capua, G.; Femia, N.; Maffucci, A.; Ventre, S. Control-Oriented Optimization of Coil Pair Design in Dynamic WPT Systems for Electrical Vehicles. In Proceedings of the 18th International Conference on Synthesis, Modeling, Analysis and Simulation Methods and Applications to Circuit Design (SMACD), Villasimius, Italy, 12–15 June 2022. [CrossRef]
19. Benalia, N.; Laroussi, K.; Benlaloui, I.; Kouzou, A.; Bensalah, A.-D.; Kennel, R.; Abdelrahem, M. Optimized Power Pads for Charging Electric Vehicles Based on a New Rectangular Spiral Shape Design. *Sustainability* **2023**, *15*, 1230. [CrossRef]
20. Maffucci, A.; Ventre, S.; Delgado Exposito, A. Impact of the Pad Geometry on System-Level Performance Indicators for IPT Systems in Electrical Vehicles. In Proceedings of the International Conference on SMACD and 16th Conference on PRIME (SMACD-PRIME), Online, 19–22 July 2021. Available online: https://ieeexplore.ieee.org/document/9547932 (accessed on 18 March 2026).
21. Di Capua, G.; Femia, N.; Stoyka, K.; Di Mambro, G.; Maffucci, A.; Ventre, S.; Villone, F. Mutual Inductance Behavioral Modeling for Wireless Power Transfer System Coils. *IEEE Trans. Ind. Electron.* **2021**, *68*, 2196–2206. [CrossRef]
22. Di Capua, G.; Maffucci, A.; Stoyka, K.; Di Mambro, G.; Ventre, S.; Cirimele, V.; Freschi, F.; Villone, F.; Femia, N. Analysis of Dynamic Wireless Power Transfer Systems Based on Behavioral Modeling of Mutual Inductance. *Sustainability* **2021**, *13*, 2556. [CrossRef]
23. Delgado, A.; Di Capua, G.; Stoyka, K.; Shi, L.; Femia, N.; Maffucci, A.; Ventre, S.; Alou, P.; Oliver, J.A.; Cobos, J.A. Self and Mutual Inductance Behavioral Modeling of Square-Shaped IPT Coils with Air Gap and Ferrite Core Plates. *IEEE Access* **2021**, *10*, 7476–7488. [CrossRef]
24. Di Capua, G.; Maffucci, A.; Capriglione, D.; Di Mambro, G.; Femia, N.; Oliva, N.; De Guglielmo, L. Mutual Inductance Modeling for the Analysis of the Impact on Wireless Power Transfer Systems. In Proceedings of the 2024 IEEE International Symposium on Measurements & Networking (M&N), Rome, Italy, 2–5 July 2024. [CrossRef]
25. Stoyka, K.; De Guglielmo, L.; Di Capua, G.; Femia, N. Transmitter Input Current Modeling in Electric Vehicles Dynamic Charging IPT Systems. In Proceedings of the 2020 27th IEEE International Conference on Electronics, Circuits and Systems (ICECS), Glasgow, UK, 23–25 November 2020. [CrossRef]

26. Di Capua, G.; De Guglielmo, L.; Femia, N. Performance Analysis of IPT Systems for Electric Vehicles Dynamic Battery Charging. In Proceedings of the International Conference on SMACD and 16th Conference on PRIME (SMACD-PRIME), Online, 19–22 July 2021. Available online: https://ieeexplore.ieee.org/document/9547930 (accessed on 18 March 2026).
27. Di Capua, G.; Femia, N. Optimal Coils and Control Matching in Wireless Power Transfer Dynamic Battery Chargers for Electric Vehicles. *IEEE Access* **2021**, *9*, 166542–166551. [CrossRef]
28. Zhu, J.; Barmada, S.; Ceraolo, M.; Fontana, N.; Musolino, A. Resonant coil matrix shielding for dynamic WPT systems. *Int. J. Appl. Electromagn. Mech.* **2024**, *76*, 181–196. [CrossRef]
29. Fontana, N.; Simonazzi, M.; Sandrolini, L.; Monorchio, A.; Barmada, S. Analysis and Design Considerations of Nonhomogeneous Metamaterial for Low-Frequency Magnetic Field Shielding. *IEEE Trans. Electromagn. Compat.* **2025**, *67*, 1490–1501. [CrossRef]
30. Dehui, W.; Chao, H.; Fan, Y.; Qisheng, S. Analytical calculations of self- and mutual inductances for rectangular coils with lateral misalignment in IPT. *IET Power Electron.* **2019**, *12*, 4054–4062. [CrossRef]
31. Leng, Y.; Luo, D.; Li, Z.; Yu, F. Analysis of Mutual Inductance Characteristics of Rectangular Coils Based on Double-Sided Electromagnetic Shielding Technology and Study of the Effects of Positional Misalignment. *Electronics* **2025**, *14*, 200. [CrossRef]
32. Di Capua, G.; Femia, N.; Di Mambro, G.; Maffucci, A. Data-Driven Behavioral Modeling of Mutual and Self-Inductance in Wireless Power Transfer Coils. In Proceedings of the 2026 International Conference on Synthesis, Modeling, Analysis and Simulation Methods and Applications to Circuit Design (SMACD), Dresden, Germany, 29 June–2 July 2026.
33. *IEEE Std C95.1-2005*; Standard for Safety Levels with Respect to Human Exposure to Radio Frequency Electromagnetic Fields, 3 kHz to 300 GHz. IEEE: Piscataway, NJ, USA, 2006. [CrossRef]
34. ICNIRP. Guidelines for Limiting Exposure to Electromagnetic Fields (100 kHz to 300 GHz). *Health Phys.* **2020**, *118*, 483–524. [CrossRef]
35. *IEC 61980-1:2020*; Electric Vehicle Wireless Power Transfer (WPT) Systems—Part 1: General Requirements. International Electrotechnical Commission: Geneva, Switzerland, 2020. Available online: https://webstore.iec.ch/en/publication/31657 (accessed on 18 March 2026).
36. Triviño-Cabrera, A.; González-González, J.M.; Aguado, J.A. *Wireless Power Transfer for Electric Vehicles: Foundations and Design Approach*; Springer: Cham, Switzerland, 2020. [CrossRef]
37. Campi, T.; Cruciani, S.; Maradei, F.; Feliziani, M. Magnetic Field Mitigation by Multicoil Active Shielding in Electric Vehicles Equipped with Wireless Power Charging System. *IEEE Trans. Electromagn. Compat.* **2020**, *62*, 1398–1405. [CrossRef]
38. Kim, J.; Kim, J.; Kong, S.; Kim, H.; Suh, I.S.; Suh, N.P.; Cho, D.-H.; Kim, J.; Ahn, S. Coil Design and Shielding Methods for a Magnetic Resonant Wireless Power Transfer System. *Proc. IEEE* **2013**, *101*, 1332–1342. [CrossRef]
39. Rong, C.; Wang, Y.; Chen, M.; Lu, Y.; Wu, Z.; Xia, C.; Liao, Z.; Liu, X. A Comprehensive Analysis of Metamaterial-Coupled WPT Systems for Low Electromagnetic Field Leakage. *IEEE Trans. Electromagn. Compat.* **2023**, *65*, 166–176. [CrossRef]
40. Brizi, D.; Fontana, N.; Barmada, S.; Monorchio, A. An Accurate Equivalent Circuit Model of Metasurface-Based Wireless Power Transfer Systems. *IEEE Open J. Antennas Propag.* **2020**, *1*, 549–559. [CrossRef]
41. Brizi, D.; Fontana, N.; Tucci, M.; Barmada, S.; Monorchio, A. A Spiral Resonators Passive Array for Inductive Wireless Power Transfer Applications with Low Exposure to Near Electric Field. *IEEE Trans. Electromagn. Compat.* **2020**, *62*, 1312–1322. [CrossRef]
42. Barmada, S.; Fontana, N.; Sandrolini, L.; Simonazzi, M. Analysis of Current Distribution and Termination Conditions in 2D Metasurfaces. *COMPEL-Int. J. Comput. Math. Electr. Electron. Eng.* **2024**, *43*, 427–443. [CrossRef]